

UNIVERSITY OF THE WESTERN CAPE  
FACULTY OF SCIENCE

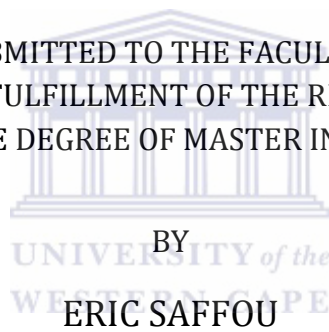
---

DEPARTMENT OF APPLIED GEOLOGY



# NUMERICAL ANALYSIS OF FINITE STRAIN IN THE WARM ZAND STRUCTURE

A THESIS SUBMITTED TO THE FACULTY OF SCIENCE  
IN PARTIAL FULFILLMENT OF THE REQUIREMENTS  
FOR THE DEGREE OF MASTER IN SCIENCE



BY  
ERIC SAFFOU

SUPERVISOR

PROFESSOR JAN VAN BEVER DONKER

CO-SUPERVISOR

Dr BAILIE

July 2014

## ABSTRACT

This research project had two different parts: The first was about the mapping of a section of the Warm Zand Structure and the collection of strain data. The second part focused on the analysis of the finite strain and strain pattern in the Warm Zand Structure. The Warm Zand Structure consists of strongly deformed calc-silicates of the Puntsit formation and feldpathic quartzites of the Goede Hoop formation which gradually change into pure quartzites in some locations. The second phase of folding  $F_2$  in the calc-silicates gave open folds. Strain markers are very scarce in the Warm Zand Structure; on the Emmanuel Farm pebbles were not found. However on the Compion Farm, pebbles are scattered and occur in few number. In the study area boudins were found in loose rocks hence they could not be used to estimate orientation of the XY plane of the strain ellipsoid (Ramsay, 1967). Folds on the other hand was common and was used to investigate the bulk shortening of the rocks and to understand the kinematical folding mechanisms involved in the folding process of the rock in the Warm Zand Structure. The strain contour map and the Sherwin and Chapple graph were used to investigate the strain and viscosity contrast respectively. The viscosity contrast of the folds collected in the Puntsit falls between 100-53 whereas the bulk shortening on the other hand is between 60-53%. The values of the shortening found agree with those found by van Bever Donker (1980). The numerical modelling on the other demonstrated that in addition to layer parallel shortening and the flattening mention by van Bever Donker (1980) Tangential Longitudinal Strain and Flexural Flow are also involved in the folding process of the fold collected in the Puntsit Formation.

## ACKNOWLEDGEMENTS

I wish to express my sincere appreciation and deep gratitude to my supervisor Professor Jan Van Bever Donker, for his academic guidance and valuable comments during this research program. This work would be incomplete without his professional support and encouragement.

I would also like to thank my co-supervisor Dr Bailie for his assistance and the time to review my work.

I would like to express a special thanks for the help from Professor Jesus Aller, Professor Fernando Bastida and Professor Nilo Bobillo-Ares from the Fold Modelling Research Group of University of Oviedo in Spain for their comments and technical assistance in numerical modelling of folds.

The financial support of INKABA Ye Africa through the award of a bursary to conduct this work is sincerely acknowledged.



A special thanks for my cousin Laurent and his wife Lizenda for their hospitality and moral support.

My final and special profound gratitude is to my wife Ellen and my dearest parents for their outstanding kindness and patience.

<b>INTRODUCTION.....</b>	<b>9</b>
<b>GEOLOGY OF THE KAKAMAS TERRANE.....</b>	<b>11</b>
2.1 Introduction.....	11
2.2 Lithologies of the Kakamas Terrane .....	13
2.3 Structures and Metamorphism .....	14
2.3 Evolution of the Kakamas Terrane .....	16
<b>GEOLOGY OF THE STUDY AREA.....</b>	<b>18</b>
3.1 Structural Geology of the Warm Zand Structure .....	18
3.2. Description of the Main Lithologies of the Study Area .....	18
3.2.1 The Goede Hoop Formation.....	19
3.2.2) The Puntsit Formation.....	22
3.3) Strain Markers in the Study Area .....	25
<b>INVESTIGATION OF STRAIN AND VISCOSITY CONTRAST FROM FOLDS.....</b>	<b>26</b>
4.1 Introduction.....	26
4.2 Strain Contour Map.....	29
4.3 Results and Interpretations.....	33
5.1 Introduction.....	41
5.2) Mathematical Analysis of a Layer Folded by TLS .....	43
5.3.1) Fourier Series .....	45
5.3.2) Conic Sections .....	47
5.3.2) Power Functions.....	52
5.3.3) Sub-ellipses and Super-ellipses .....	53
5.3.4. Cubic Bézier Curves .....	54
4.4 Results and Interpretations.....	55
4.4.1) Conic Sections .....	55
4.4.2) Power Function .....	56
4.4.3) Sub-ellipses and Super-ellipses & Bézier curves .....	56
<b>MATHEMATICAL MODELLING OF FOLD KINEMATIC MECHANISMS AND SIMULATION OF STRAIN PATTERN.....</b>	<b>66</b>
6.1 Introduction.....	66





<b>6.2 Mathematical Description of Kinematic Folding Mechanisms .....</b>	<b>67</b>
6.2.1 Tangential Longitudinal Strain (TLS) .....	67
6.2.2 Flexural Flow (FF) .....	68
6.2.3 Initial Layer Shortening (ILSH) and Flattening (FL) .....	69
<b>6.2 Numerical Simulation of folds .....</b>	<b>70</b>
<b>6.3 Results and Interpretations.....</b>	<b>72</b>
 <b>CONCLUSIONS .....</b>	 <b>78</b>
<b>7.1 Future Research .....</b>	<b>79</b>
<b>REFERENCES.....</b>	<b>80</b>



## LIST OF TABLES

Table 2.1. Major subdivision of the Namaqua Sector .....	12
Table 2.2 Lithology of Biesjepoort Subgroup .....	15
Table 4.1. Fold Shape Parameters (multiplied by 1000).....	33
Table 4.3. Strain partitioning analysis of fold1 .....	40
Table 5.1. Fold shape parameter obtained from fold profiler® using the conic section .....	58
Table 5.2. Fold shape parameter obtained from fold profiler using power function method .....	60
Table 5.3 Fold shape parameters obtained using ébiezer curve method ble 5.3 fold shape parameters obtained using ébiezer curve method.....	62
Table.5.4 Fold shape parameter obtained from sub-ellipses and super-ellipses method .....	64

## LIST OF FIGURES



fig.2.1: Map of Southern Africa. Modified after cornell et al. (2006) .....	13
Fig.3.1 Map of the Warm Zand Structure .....	19
Fig.3.3. Different types of calc-silicate rocks found in the warm zand area (a) epidotised banded calc-silicate rock; (b) moderately foliated dark calc-silicate rocks dipping se; (c) calc-silicate rock rich in piedmontite (reddish colour); (d) quartzitic banded calc-silicate rock.....	23
fig.3.4. (a) Weathered wollastonite in calc-silicate rocks; (b) Pinch-and –swell structures of amphibolite in amphibolite pure; (c) Multilayer folding in the calc-silicates; (d) Boudins of calc-silicates in carbonate rocks.....	24
Fig.4.1 (a) Fold parameters used in strain analysis: arc length (larc), wavelength ( $\lambda$ ), amplitude (a) and thickness (h).....	26
Fig.4.2. Different stages of folding (Schmalholz and Podladchikov, 2000).....	29
Fig.4.3. Estimation of Viscosity Contrast of Fold .....	37
Fig.4.4. Strain of viscosity ratio of fold 1. (a) Fletcher and sherwin (1978). (b) Schmalholz and Podladchikov (2001). a- amplitude, h- thickness, $\lambda$ – wavelength, $\beta^*$ relative band width of amplitude spectrum and $L_p$ – preferred wavelength .....	38

Fig.4.5. Graph of viscosity ratio of fold 11. (a) Fletcher and Sherwin (1978). (b) Schmalholz and Podladchikov (2001). a- amplitude, h- thickness, $\lambda$ – wavelength, $\beta^*$ relative band width of amplitude spectrum and $L_p$ – preferred wavelength. ....	39
fig.4.6. Strain partitioning analysis. (a) Picture of fold 9. (b) Strain contour map of fold 9. blue dots represent individual strain and red dots bulk strain. (c) Table 4.2. strain partitioning analysis of fold 9. (d) picture of fold 1. (b) Strain contour map of fold 1. blue dots represent individual strain and red dots bulk strain. (f) Strain partitioning analysis of fold 1. ....	40
Fig.5.1: a) Tangential longitudinal strain and curvature of the neutral line $k$ ; $\theta$ being the angle between the tangent line at $p$ and the positive $x$ -axis; b) small increment in $x$ and $y$ direction respectively named $\delta x$ and $\delta y$ . $\delta s$ is the hypotenuse of the triangle formed by $\delta x$ and $\delta y$ and which is the change in arc-length along the curve; c) geometrical analysis of the nl after folding. (1) neutral before folding. (2) neutral line after folding $p$ and $q$ are transformed into $p'$ and $q'$ . (n.c. bobillo-ares et al 2000) .....	42
Fig.5.2.(a) Hudleston diagram (1979). (b) Definition of conic section. (c) Fold profile: $h$ , hinge point; $i$ , inflection point; $a$ , area beneath the limb profile; $\acute{a}$ , maximum dip. (d) Description of the aspect ratio of a fold limb. (e) The description of the normalized of a fold limb. (lisle et al.,2006) .....	46
Fig. 5.5. Fold shape of the punsit formation analysed by fold profiler.....	49
Fig. 5.6. Fold shape of the punsit formation analysed by fold profiler.....	50
Fig. 5.7. Simplified cubic bézier curve used to analyse fold shapes (after srivastava and lisle, 2004.) .....	55
Fig. 5.8. Analysis of the fold 1-10 using conic section method. (a) graph of the aspect ratio versus the eccentricity ( $e$ ); (b) graph of the aspect ratio versus the normalised area.....	59
Fig. 5.9. Analysis of the folds 1-10 using power functions method. (a) graph of the aspect ratio versus the shape parameter $n$ ; (b) graph of the aspect ratio versus the normalised area.....	61
Fig. 5.10. Analysis of the <b>folds 1-10</b> using sub-ellipses and super-ellipses method. (a) Graph of the aspect ratio versus the shape parameter $p$ ; (b) Graph of the aspect ratio versus the normalised area. ....	63
Fig. 5.11. Analysis of the folds 1-10 by fold profiler using cubic bézier curves method. (a) Graph of the aspect ratio versus the shape parameter $l$ ; (b) Graph of the aspect ratio versus the normalised area.....	65
Fig.6.1. (a) Geometrical changes experienced by the guide line (GL) during tangential longitudinal strain (TLS). (b) Gometrical changes experienced by the guide line (GL) during flexural flow (FF)(aller et al., 2004).....	67
Fig.6.2. Geometrical changes experienced by the guide line (GL) flattening (FL) or initial layer shortening (ILSH) (aller et al., 2008). ....	69
Fig.6.3 Elements used in the numerical modelling of a fold (aller et al., 2004) .....	71
Fig.6.4. Best fit for fold 1 using simulation. (a) Elliptical folds formed in the calc-silicates in the warm zand structure. (b) Input data characterising the theoretical fold (block1, block2, block3), and comparison of	

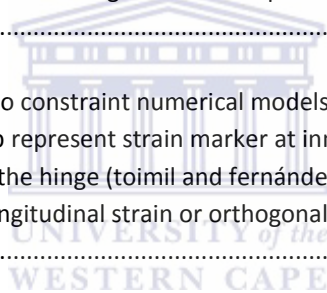
some outputs of the theoretical fold with the corresponding parameters of the natural fold. (c) Folded configuration of the theoretical layer showing the strain ellipse and shading proportional to the aspect ratio of the strain ellipses. .... 73

Fig.6.5. Best fit for natural fold 2 using simulation. (a) Parabolic folds formed in the calc-silicates in the warm zand structure. (b) Input data characterising the theoretical fold (block1, block2, block3), and comparison of some outputs of the theoretical fold with the corresponding parameters of the natural fold. (c) Folded configuration of the theoretical layer showing the strain ellipse and shading proportional to the aspect ratio of the strain ellipses. .... 73

fig.6.6. Best fit for fold 3 using simulation. (a) Hyperbola folds formed in the calc-silicates in the warm zand structure. (b) Input data characterising the theoretical fold (block1, block2, block3), and comparison of some outputs of the theoretical fold with the corresponding parameters of the natural fold. (c) Folded configuration of the theoretical layer showing the strain ellipse and shading proportional to the aspect ratio of the strain ellipses ..... 74

Fig.6.7. Best fit for fold 9 using simulation. (a) Parabolic folds formed in the calc-silicates in the Warm Zand Structure. (b) Input data characterising the theoretical fold (block1, block2, block3), and comparison of some outputs of the theoretical fold with the corresponding parameters of the natural fold. (c) Folded configuration of the theoretical layer showing the strain ellipse and shading proportional to the aspect ratio of the strain ellipses. .... 74

Fig. 6.8.(a) Location of strain data used to constraint numerical models. the data must be sampled on the hinge and limbs of the fold. point q and p represent strain marker at inner arc and outer respectively. section a shows the position of cleavage on the hinge (toimil and fernández, 2007). (b) Deformation pattern of pebbles deformed by tangential longitudinal strain or orthogonal flexure and flexural flow (fossen, 2010, p. 233) ..... 75



---

# Chapter 1

---

## Introduction

The Namaqua Sector is composed of NNW-SSE, NW to SE and finally EW oriented terranes. Those Terranes are coeval with the Mesoproterozoic tectonic events which led to the formation of the Rodina at around 1.1 Ga (Dalziel., 1991). The Kakamas Terrane is located in the western part of the Namaqua sector and it is characterized by amphibolite grade supracrustal rocks such as metapelite, mature quartzite and calc-silicates intruded by granitoids. Four different fold phases have been recognized in the Kakamas Terrane, the interference between  $D_2$  and  $D_3$  results in the formation of the Warm Zand Dome referred in this study as the Warm Zand Structure. Van Bever Donker (1983) mapped three shear zones in the Kakamas Terrane. The Kakamas shear zone characterized by narrow parallel zone of porphyroblastesis, the Neusspruit lineament in the other hand is characterized by a pronounced topographic expression due to the hard platy quartz-mica schist and the termination of feldspathic quartzite and finally Brakfontein shear zone which is recognized by drag features and minor displacement in the massive feldspathic quartzite. A study of the variation of the strain in the Kakamas Terrane conducted by van Bever Donker(1980) showed that the strain ellipsoid becomes more flattened, slightly less oblate between Neusspruit lineament and the Kakamas shear zone, and finally slightly change to prolate in the Warm Zand dome. The fabric analyses of quartz c-axes showing a small-girdle together with the prolate strain ellipsoid indicate that The Warm Zand dome had experienced a constrictive strain.

In this study we are going to use the strain contour map (Schmalholz and Podladchikov, 2001) to estimate the strain from folds in the Warm Zand Structure. The strain contour map allows us to overcome the obstacle of the unknown initial geometry when using folds as strain markers to evaluate the strain. Furthermore van Bever Donker (1980) only recognized through field observations flattening and layer parallel shortening as fold kinematic mechanisms involve in the folding process that took place in the Warm Zand Structure. Bobillo-Ares et al (2004) show on the other hand that folds are produced by simultaneous or superpose folding kinematic mechanisms which result in a specific strain pattern. Another objective of this research will be to investigate the order and the intensity at which kinematic folding mechanisms which might have been involved in the folding process in the Warm Zand Structure. This will be demonstrated by investigating the strain pattern of folds in the area of interest. The strain pattern is the order in which the folding kinematic mechanisms occur during the folding process. The strain pattern cannot be observed in field but can be study through numerical simulation.

To present the work introduced above, this thesis is divided into seven chapters. Chapter 2 gives an overview of the geology of the Kakamas Terrane located in the Namaqua sector of Namaqua-Natal province. Chapter 3 presents a detailed geology of the Warm Zand Structure. Chapter 4 in the other hand is an introduction to the numerical modelling of the strain pattern of the folds in the study area; it focuses on finding parameters that control the geometry of fold using mathematical modelling of fold profiles. Chapter 5 deals with the results and interpretation of the simulation of folds. In chapter 6 we summarise the main conclusion of this study and underline how the results obtained during this research can improve our understanding of the geology of the Kakamas Terrane.

---

# Chapter 2

---

## Geology of the Kakamas Terrane

### 2.1 Introduction

The Namaqua Natal Province embraces the highly deformed Mesoproterozoic igneous and metamorphic rocks formed during the Namaqua Orogeny. It extends for 1400 km across South Africa and Namibia and is a 400 km wide arcuate orogenic belt bordering the Archean Kaapvaal Craton to the south and southwest and truncated by ~600 Ma Pan-African belts in the west and south (Fig.2.1) The Namaqua Natal Province is composed of tectono-stratigraphic terranes bounded by shear zones; the three main lithostratigraphic components of the Namaqua Natal Province are:

- The late Paleoproterozoic reworked Kheisian rocks
- Mesoproterozoic juvenile supracrustal rocks and plutonic rocks formed during the Namaquan Wilson cycle ~1600 to 1200 Ma ago, and assembled during the Namaqua Orogeny, accompanied by intense deformation and metamorphism
- Syn- and post-tectonic granitoids formed between 1200 and 1000 Ma in addition to a number of scattered small mafic/ultramafic intrusions (Thomas et al., 2006)

The Namaqua Sector of the Namaqua-Natal Province is a well exposed Mesoproterozoic, low–pressure, amphibolite–granulite terrane flanking the Archean Kaapvaal craton of southern Africa (Robb et al., 1999).

Five domains had been recognised within the Namaqua sector (Table 2.1); from west to east these are: the Richtersveld Subprovince, Bushmanland Terrane, Kakamas Terrane, Areachap Terrane and Kaaien Terrane (Thomas et al., 1994). Table 2.1 gives a summary of the characteristics of each of the five domains. The Kakamas Terrane will be further described in the following paragraphs.

**Table 2.1. Major subdivision of the Namaqua Sector**

<b>MAJOR SUBDIVISIONS OF THE NAMAQUA SECTOR</b>	
<b>Richtersveld Subprovince</b>	~2000 Ma low-to medium-grade supracrustal rocks and intrusions in the northwestern Namaqua Sector; much less affected by the Namaqua–Orogeny. Surrounded by the Namaqua high grade Bushmanland and Kakamas Terranes.
<b>Bushmanland Terrane</b>	2000 Ma granite gneisses; 1600 to 1200Ma amphibolite to granulite grade supracrustal rocks and 1200 to 1000 Ma granitoids.
<b>Kakamas Terrane</b>	Possible ~2000 Ma supracrustal metapelite, Namaqua granitoids and Namaqua fabric. It is bounded in the east by the Boven Rugzeer shear zone
<b>Areachap Terrane</b>	Juvenile ~1300 Ma arc-related supracrustal rocks and 1000 Ma granitoids. The Areachap-Kakamas terrane boundary diverges from the Boven Rugzeer Shear Zone in the south. The eastern boundary is the Brakbosch-Trooilapspan Shear Zone
<b>Kaaïen Terrane</b>	Metaquartzite, deformed early Namaqua volcano-sedimentary rocks and undeformed, metamorphosed, bimodal volcanic rocks. The Dabep Thrust forms the eastern boundary

The Kakamas Terrane lies to the east of the Bushmanland Terrane. It stretches northwards across the Orange River into Namibia and southwards towards Kenhardt-Putsonderwater.



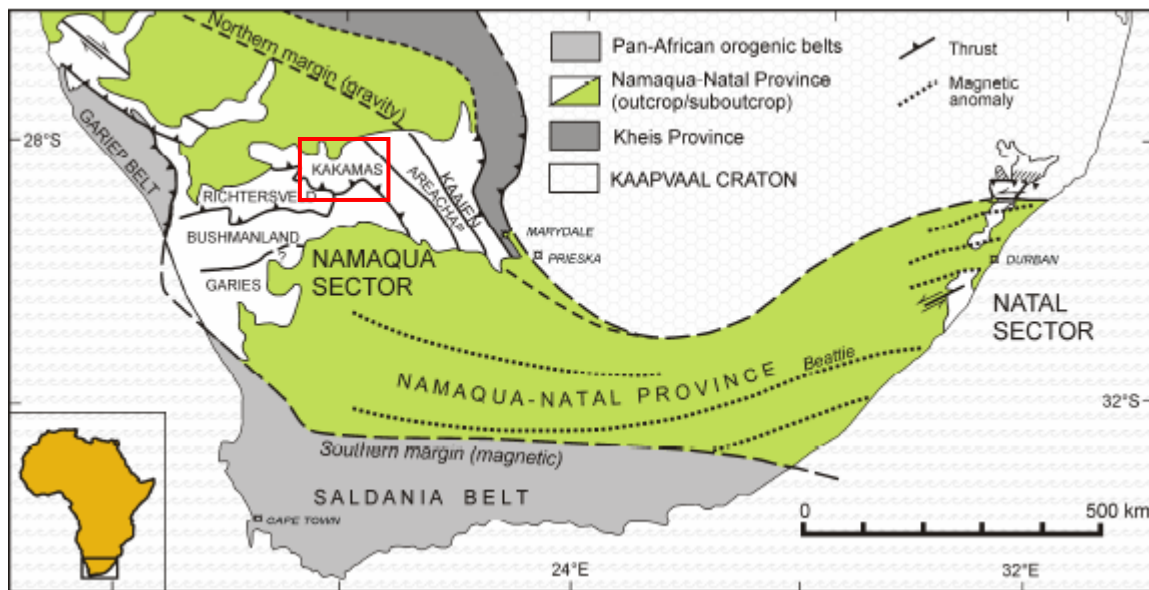


Fig.2.1: Map of Southern Africa. Modified after Cornell et al. (2006)

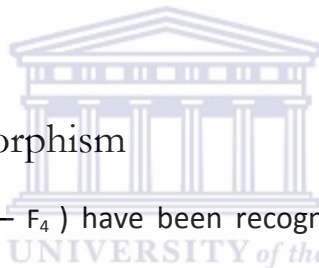
In the east it is in contact with the Areachap terrane along the Boven Rugzeer Zone and is bounded by the Hartbees River Thrust to the west and the Swartrand fault to the northwest (Thomas et al., 2006). The Kakamas Terrane consists of amphibolite grade supracrustal rocks such as metapelite, quartzite and calc-silicate. Large parts of the area are intruded by pre-, syn- and post tectonic granitoids.

## 2.2 Lithologies of the Kakamas Terrane

The lithologies of the Kakamas Terrane (Fig.2.1) are dominated by the rocks of the Korannaland Group (Table 2.1). The latter consists of quartz-muscovite schist and calc-silicates, quartzofeldspathic gneisses, amphibolite gneisses and biotite gneiss. Apart from the unquestionable positioning of the Goede Hoop Formation at the top of sequence a clear stratigraphic order has not been established for the various units (Van Bever Donker, 1983). The muscovite-bearing quartzite of this formation overlies the dark-weathering calc-silicate rocks of the Punsit Formation which, in turn, is underlain by the quartzofeldspathic gneiss of the Riemvasmaak Gneiss, which intrudes the metasedimentary succession. The Goede Hoop

and Puntsit formations are separated by the reddish to grey quartzofeldspathic gneiss of the Rautenbach se Kop Formation (Moen, 2007). The latter can be differentiated from the Riemvasmaak Gneiss by the absence of augen and has a darker colour. The brown-to grey-weathering medium grained quartz-feldspar-biotite gneiss is separated from the Sandputs Formation by the Friersdale Charnockite, which shows an intrusive character with the country rock. Different mechanisms have been suggested regarding the origin and the mode of emplacement of the Friersdale charnockite.

Van Bever Donker (1980) and Van Zyl (1981) showed that contamination and assimilation of country rocks by a granitic magma could explain the chemical range in the charnockitic adamellite



### 2.3 Structures and Metamorphism

Four phases of deformation ( $F_1 - F_4$ ) have been recognized, the first phase  $F_1$  is mainly characterized by penetrative axial plane-foliation.  $F_1$  structures were transposed by late deformations hence they are almost invisible in the terrane.  $F_2$  structures however are dominant throughout the area. The main foliation  $F_1$  is refolded during  $F_2$  deformation and the fold types are generally tight folds. The trends of  $F_2$  axial planes are usually north-west-south-east, dipping between 30-35 degree while the trend of fold axes of folds formed during  $F_3$  is north east (van Bever Donker., 1983). Domal structure such the Warm Zand Structure formed due to the interference between  $F_2$  and  $F_3$ . The final deformation  $F_4$  is mainly characterized by the appearance of kink folds in several places in the Kakamas Terrane

Table 2.2 Lithology of Biesjepoort Subgroup

Lithology of the Kakamas Terrane			
KORANNALAND GROUP	Biesjepoort Subgroup	Formations	Descriptions
		Goede Hoop Formation	Micaceous feldspathic quartzite
		Valsvlei Formation	Yellow-weathering, quartz-rich gneisses
		Ganzenmond Formation	Brown to grey-weathering, medium-grained quartz-feldspar-biotite $\pm$ garnet $\pm$ sillimanite gneiss
		Rautenbach se kop Formation	Reddish to grey quartzofeldspathic gneiss
		Puntsit Formation	Dark weathering calc-silicate rocks; presence of porphyroclasts of wollastonite and diopside
		Toeslaan Formation	Aluminous gneiss (kinzigite) associated with garnetiferous migmatite
		Sandputs Formation	Feldspathic quartzite with the occurrence of calc-silicate minerals
		Omdraai Formation	Well bedded semipelitic metasediments. Medium- to-fine grained quartz-feldspar gneiss; occasional presence of hornblende and little to no biotite
		Piet Rooisberg Formation	Quartz-feldspar gneiss similar to the Riemvasmaak Gneiss quartzite

Possible correlation between metamorphism events and folding phases of deformation were established. The first metamorphic ( $M_1$ ) event is characterized by the assemblage of cordierite+ biotite+ sillimanite + garnet+ quartz+ K-feldspar. The sillimanite foliation wrapping around the garnet indicates that sillimanite was present when the flattening took place.

According to van Bever Donker (1980), the flattening only took place during  $F_2$  folding phase of deformation consequently  $M_1$  coincides with  $F_2$ . Contrary to the first event  $M_1$  which is a regional type of metamorphism the second metamorphism even  $M_2$  is a contact type of metamorphism. It is characterized by two paragenesis. The first one was formed in the north-eastern part of the terrane and it is composed of garnet + cordierite + biotite + sillimanite + staurolite + chlorite+ quartz. The second assemblage occur in the Zoovoorby schist (van Bever Donker (1980) and is made up of garnet + biotite + muscovite + Staurolite+ sillimanite + quartz. The Zoovoorby schist was identified by two mica-schist with pronounced staurolite and tourmaline crystals. As a result of the intrusion of granitoid in the calcisilicates wollastonite formed. The timing of the intrusion is assumed to be post  $F_2$  because the parts of  $F_2$  structures are only affected on that part of their rocks that have been assimilated. The third metamorphic event  $M_3$  is regarded as a low grade metamorphism where minerals such prehnite and pumpellyite formed.

### 2.3 Evolution of the Kakamas Terrane

The following structural model was suggested by van Bever Donker (1980). Granitic basement subsided to form a large basin of moderate depth, where pelitic sediments were first deposited, followed by a thick sequence of greywacke.

Amphibolite emplaced in the deepest part of the basin was suggested to represent sills or subaqueous lava. It is suggested that at this stage isostatic adjustment started resulting in upward movement, creating the shelf condition for the deposition of calc-silicates rich quartzites. Once deposited the cross-bedded feldspathic quartzites. Horizontal shortening resulted in the thickening during which the  $F_2$  structures developed. The Neusspruit lineament may have been the original major fault, from which the Duivelsnek and Kakamas Shear Zone representing the younger branches. The shear zones play an important role in the emplacement of the granites. The position of the granites with respect to the shear zones strongly suggest that the shear zones penetrated deep enough to enable the granitic material to move upward along them. The timing of the intrusion has been dated late  $F_2$  to post  $F_3$ .



---

# Chapter 3

---

## Geology of the Study Area

### 3.1 Structural Geology of the Warm Zand Structure

The Warm Zand Structure is a domal structure located the Kakamas Terrane which has been divided in two parts. The northern part is a synformal  $F_3$  structure. Axial plane of  $F_2$  structure is oblique respect to the Neusspruit Lineament and the Brakfontein Shear Zone so that in a northerly direction an increasing part of the  $F_2$  structure is being cut off. Folds mainly occur in the calc-silicates and they are generally isoclinal and no boudings had been observed in this part of the Warm Zand Structure. The southern part of the Warm Zand Structure is the result of the interference of  $F_2$  and  $F_3$ . The structure is classified as an antiform slightly modified by  $F_3$ . In the calc-silicate rocks the  $F_1$  and  $F_2$  are present. In some places ptygmatic flow folding and intrafolial folds are also encountered. For this study a detailed mapping of the main lithologies of the south part of Warm Zand structure was done with the aim of identifying the strain markers that will facilitate the strain analysis of the study area.

### 3.2. Description of the Main Lithologies of the Study Area

The study Area, the Warm Zand Structure, is situated between latitude -28, 7244 to -28, 7273 and longitude 20, 7499 to 20.8116. It covers the area between the Immanuel Farm (S28°44.520 E020° 45.796) and the Compior Farm (S28° 42.973; E020° 49.734). The Warm Zand [Structure](#) is bounded in the east by the Neusberg Structure and intruded in the west by the late-syn-tectonic biotite-rich Straussburg Granite and by the Charnockitic Adamellites in the south. The main lithologies consist of strongly deformed calc-silicates of the Punsit

formation and feldspathic quartzites of the Goede Hoop formation which gradually changes into pure quartzites at some locations.

### 3.2.1 The Goede Hoop Formation

Geringer (1973) proposed the term “Goede Hoop Formation” after a subdivision of the farm Biesje (Moen, 2007). The name was later approved by the SACS. Van Bever Donker (1980) used the term Neusberg Formation and subdivided it into “Neuspoort Member” and “Zwart Boois Berg Member”. In the study area, the Goede Hoop Formation is represented by muscovite bearing feldspathic quartzites.

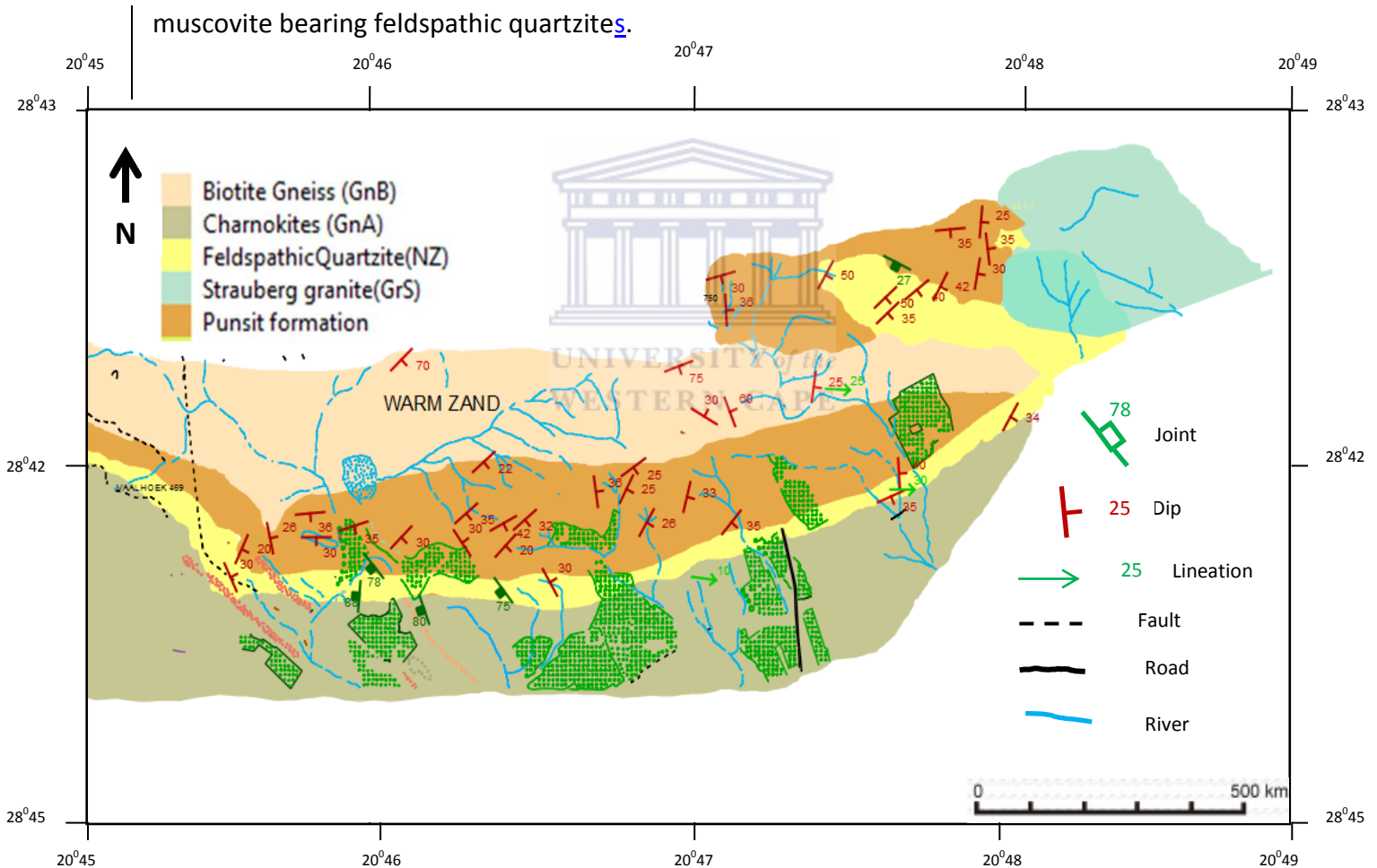


Fig.3.1 Map of the Warm Zand Structure

The thickness of the formation cannot be estimated due to difficulties in defining and locating the lower contact with the calc-silicates of the Warm Zand Structure.

On the Emmanuel Farm (S28'44.520 E020' 45.796) feldspathic quartzites are intensely fractured (Fig 3.2c) and form a hill covered in quartzite boulders. Three sets of joints striking N240°, ~N150°, and ~N80° respectively have been observed in almost every outcrop. Joint planes are occasionally filled with quartz; quartz mobilisation and trace of epidote have been observed close to the skarns. On the hand specimen, quartz, feldspar and muscovite are easily recognisable. Pebbles in the feldspathic quartzite are almost absent on this part of the Warm Zand Structure. No sedimentary structures such as cross-bedding or bedding planes have been observed, however cross-beddings have been observed at a number of localities in the Kakamas Terrane (Moen, 2007).

Muscovite-bearing quartzites grade into quartzites rich in epidote and phlogopite or into pure quartzite which are well stratified and display quartzitic banding portraying isoclinal folds (Fig 3.2d). The contact between the Puntsit Formation and the Goede Hoop Formation in the Emmanuel Farm (S28'44.520 E020' 45.796) is a gradational contact. The contact rocks are intensely deformed and are rich in feldspar, quartz, piemontite and epidote; no trace of muscovite has been found in the hand specimen.

On Compion Farm (S28' 42.973; E020' 49.734), we observed two different occurrences of mica-bearing quartzites; the feldspathic quartzite which displays a gneissic appearance and the well-stratified platy quartzites. The joints sets in the feldspathic quartzite show a similar pattern as those in Emmanuel Farm with other joints having intermediate trends. The hand specimen shows quartz, feldspar and muscovite, scattered pebbles (Fig.3.2a) while irregular horizons of matrix-supported conglomerate occur sporadically (Moen, 2007).



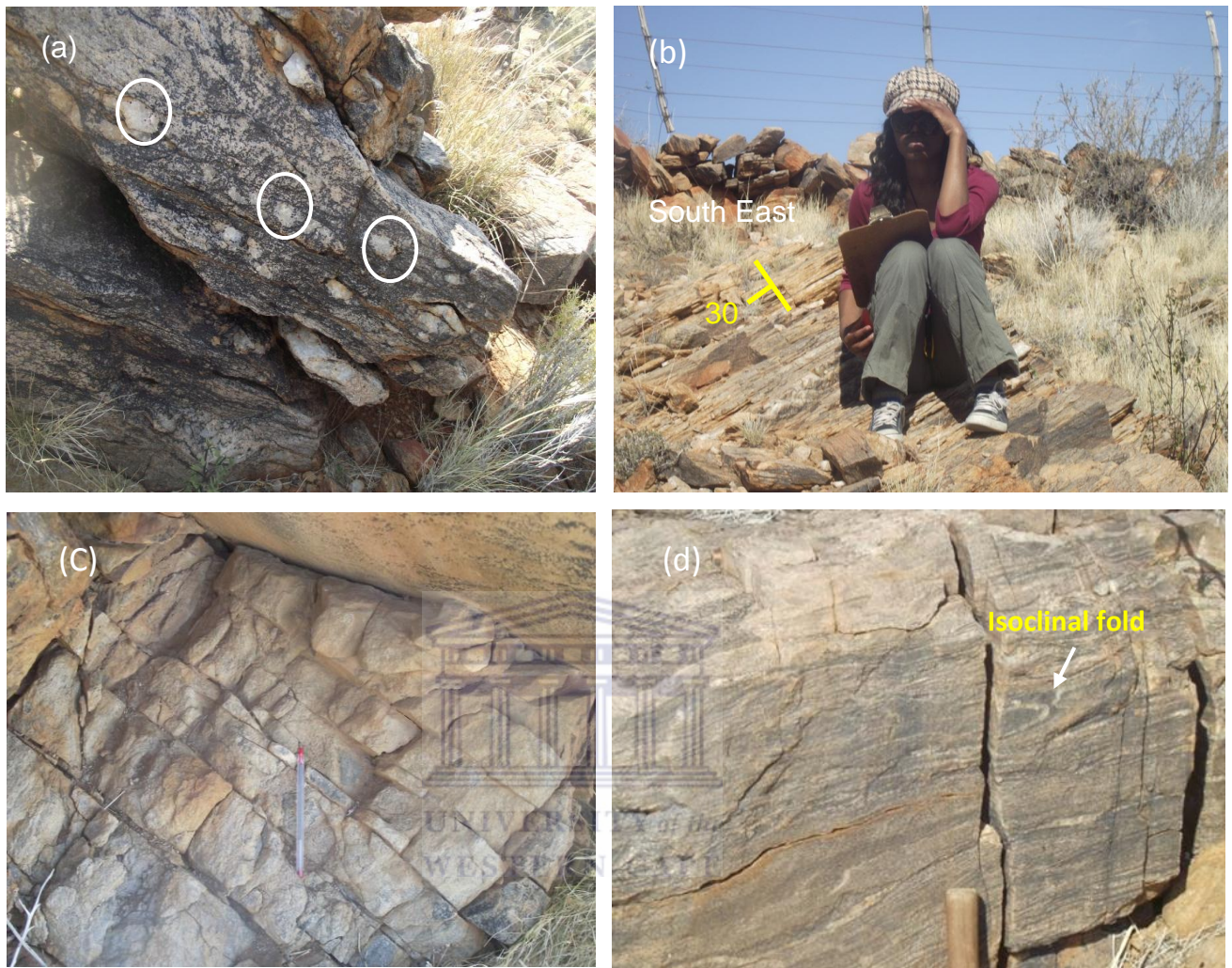


Fig.3.2 (a) Scattered pebbles in the feldspathic quartzites; (b) Feldspathic quartzites dipping 30 SE (c) Parallel fractures in the Feldspathic Quartzite ); (d) Isoclinal fold in pure quartzites.

The platy quartzites developed foliation parallel to bedding and generally dip between 35 degree south east (Fig.3.2.b). The rocks located at the gradational contact with the calc-silicates are rich in epidote, quartz, feldspar and piemontite.

### 3.2.2) The Puntsit Formation

The Puntsit Formation is overlain by muscovite bearing quartzite of the Goede Hoop Formation, and consists of dark-weathered banded calc-silicate rocks. Van Bever Donker (1980) referred to them as “Baviaans Krantz banded calc-silicate-rich quartzite”.

The calc-silicates contain a wide range of Ca-rich silicate minerals associated with plagioclase, K-feldspar, biotite, muscovite and amphibole (van Bever Donker; 1979). The thickness of the formation cannot be determined owing to difficulties in defining its lower contact and complex deformations (Moen, 2007). On the Emmanuel Farm (S28°44.520' E020°45.796'), the calc-silicate rocks occur in association with amphibolite and meta-psammites together with skarns. They are fine grained and display light- to dark-green colours. The dark calc-silicates dip southeast (Fig.3.3b) and show moderate foliation and quartzitic bands (Fig.3.3d). Quartzitic bands are generally parallel to foliation except where intrafolial folds occur. The light grey to grey rocks display epidotised bands (Fig.3.3a), regular or irregular in width. The fracture patterns occurring in the calc-silicates define a systematic set with major sets striking ~N240°, ~N150°, and ~N80° respectively. The crosscutting relationship of the fractures mostly consists of X-type intersections. This is in sharp contrast with the parallel joint sets observed in feldspathic quartzite. Well-foliated amphibolite layers are encountered frequently along with the calc-silicate metapelitic rocks. Pinch-and-swell structures (Fig.3.4b) which formed due to the competency contrast between the carbonate layers and the enclosing calc-silicates are encountered in loose outcrops.



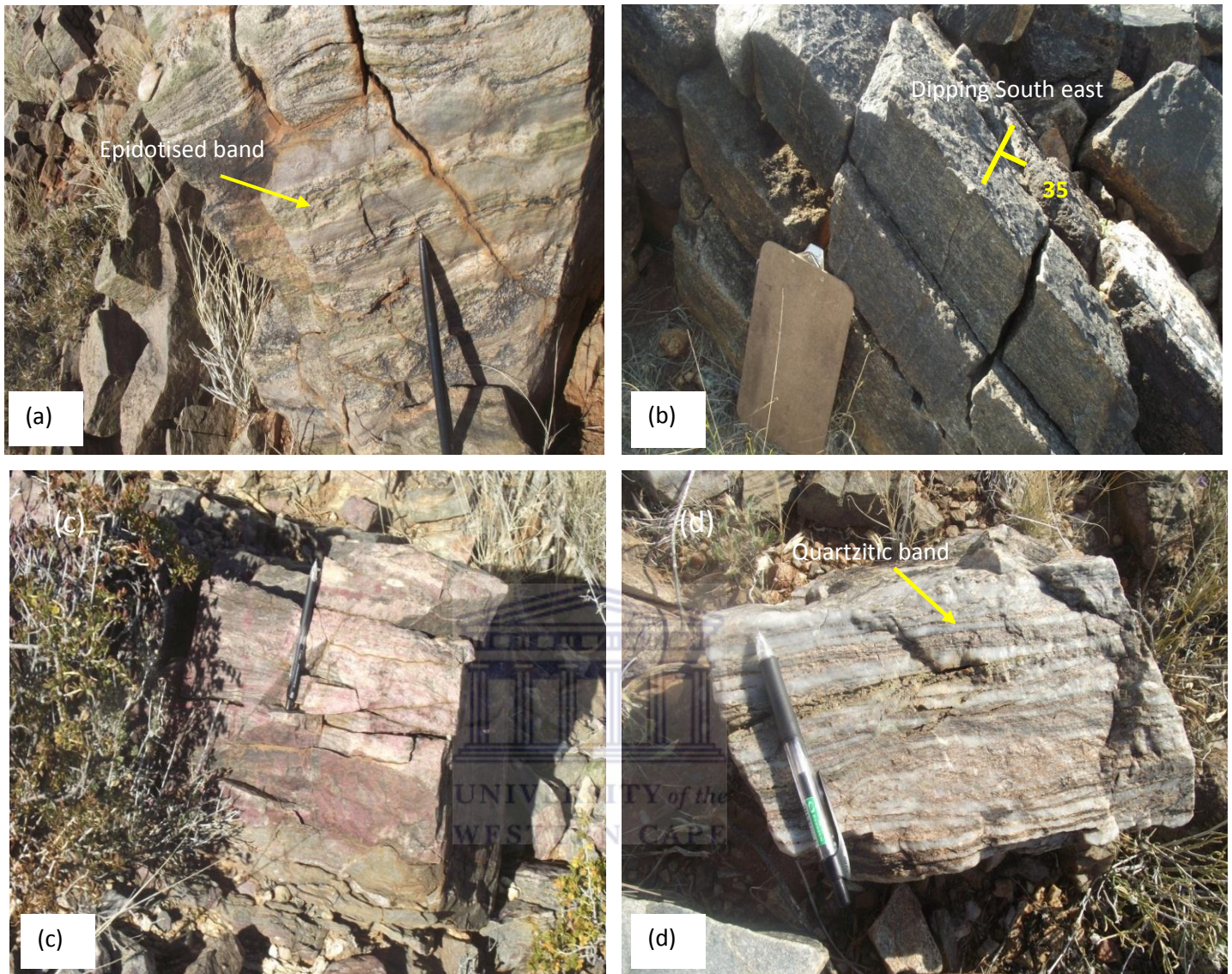


Fig.3.3. Different types of calc-silicate rocks found in the Punsit Formation (a) Epidotised banded calc-silicate rock; (b) Moderately foliated dark calc-silicate rocks dipping SE; (c) calc-silicate rock rich in Piedmontite (reddish colour); (d) quartzitic banded calc-silicate rock.



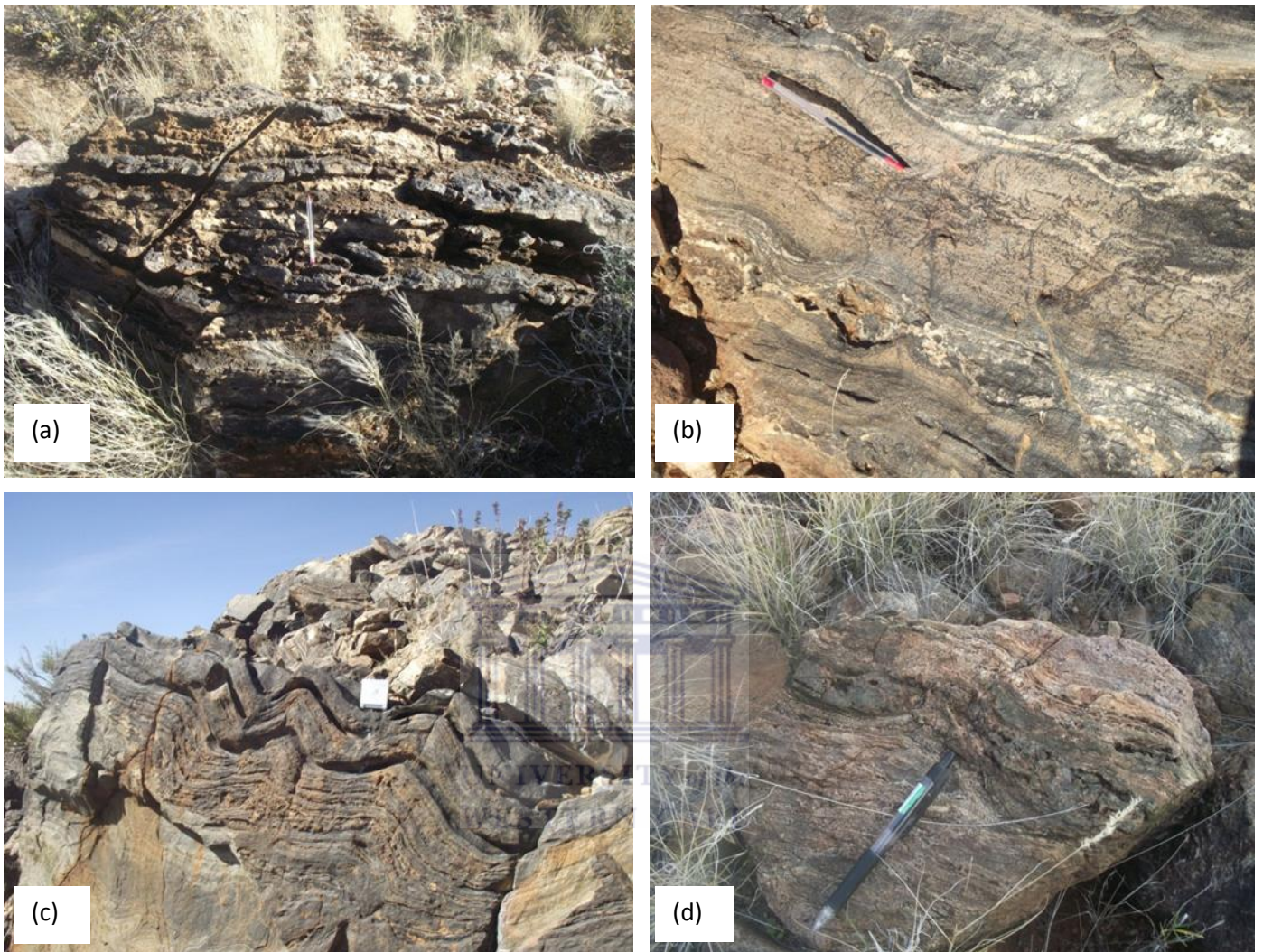


Fig.3.4. (a) Weathered wollastonite in calc-silicate rocks; (b) Pinch-and –swell structures in amphibolite rock; (c) Multilayer folding in the calc-silicates; (d) Boudins of calc-silicates in loose carbonate rocks

On the Compion Farm (S28' 42.973; E020' 49.734), calc-silicate rocks are fine grained, massive, weathered and display a wide range of colours such as dark-green, light -grey to grey and pink; the pink colour in the calc-silicates may be explained by the enrichment of calc-silicates in piedmontite(Fig.3.4c). The calc-silicates occur in association with amphibolite, metapelites, marble and carbonates.

The fracture pattern is a poorly defined systematic pattern with major sets N240°, ~N150°, and ~N80° respectively. Discontinuous fractures are also observed and show no preferential pattern. On the Compion Farm, most boudins observed are usually amphibolites enclosed in calc-silicates rocks with their shortest and longest dimension respectively perpendicular and parallel to the foliation in the enclosing rocks.

Wollastonite occurs in abundance (Fig.3.4a) and is confined to the calc-silicates. Wollastonite bands vary in thickness from few millimetres to about 4m and contain fold structures of thin layers of the surrounding amphibole-epidote rich rock (van Bever Donker, 1980). The appearance of wollastonite in the Warm Zand area may be the result of the intrusion of the charnockitic adamellites into the limestones. The calc-silicate layers exhibit spectacular single and multilayer folds which reflect the major competency contrast between the calc-silicate and the enclosing rocks.

### 3.3) Strain Markers in the Study Area

Strain markers are very scarce in the Warm Zand Structure; on the Emmanuel Farm pebbles were not found. However on the Compion Farm, pebbles are scattered and occur in few number. Pebbles are generally used to obtain the strain ellipsoid using the center- to- center method, the fry method (Fry, 1970) and the  $R_f/\phi$  method (Ramsay, 1967). In the study area boudins are found in loose rocks hence they cannot be used to estimate orientation of the XY plane of the strain ellipsoid (Ramsay, 1967). Folds on the other hand are common and will be used in this study to investigate the shortening of the rocks and to understand the kinematical folding mechanisms involved in the folding process of the rock in the Warm Zand Structure.

## Investigation of Strain and Viscosity Contrast from Folds

### 4.1 Introduction

One of the weakest aspects of the structural geology of the Warm Zand Structure and by extension of the Kakamas Terrane is the lack of knowledge of strain and rock rheology. Viscosity contrast and strain data are of great interest because they improve our understanding of the rheology of the mantle and crustal rocks (Hudleston and Lan, 1995). Furthermore they also enhance our understanding of the rock-deformation processes (Hudleston and Lan, 1995). Several authors (Biot, 1961, 1965; Ramberg, 1961; Currie et al., 1962; Fletcher, 1974; Fletcher and Sherwin, 1978; Schmalholz and Podladchikov, 2001) developed methods to analyse the strain and viscosity from fold geometry.

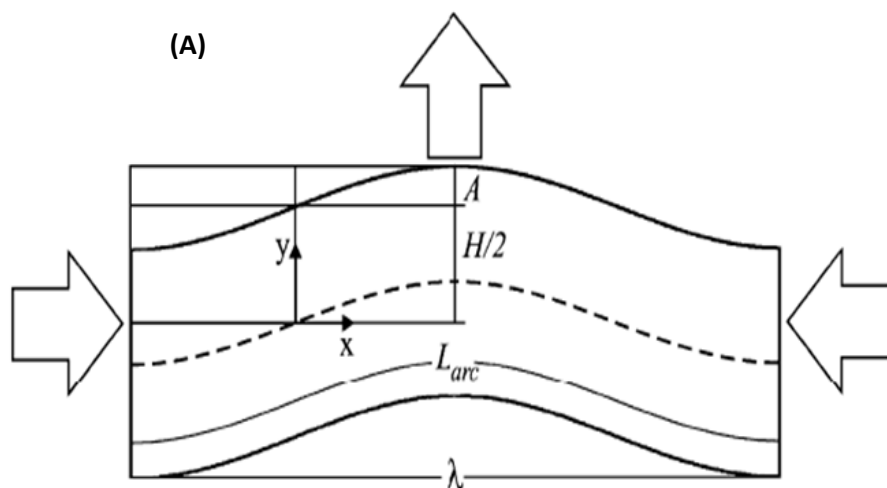


Fig.4.1 (A) Fold parameters used in strain analysis: arc length ( $L_{arc}$ ), wavelength ( $\lambda$ ), amplitude ( $A$ ) and thickness ( $H$ ).

If a layer is subjected to different sinusoidal perturbations with different wavelengths, the dominant wavelength is the wavelength associated with the perturbation that grows faster

than the other perturbations. The dominant wavelength ( $\lambda_d$ ) for Newtonian viscous layer and matrix is approximated by Biot (1961) as follows:

$$\frac{\lambda_d}{h} = 2\pi \sqrt[3]{\frac{\mu_l}{6\mu_m}} \quad (1)$$

$\mu_m$ ,  $\mu_l$ ,  $h$  and  $\lambda_d$ , are respectively, the effective viscosity of the layer, the viscosity of the matrix, the layer thickness and the dominant wavelength. When the elastic properties of rocks influence the folding, the dominant wavelength is given by Currie et al., 1962 as follows:



$$\frac{\lambda_d}{h} = 2\pi \sqrt[3]{\frac{E_l}{6E_m}} \quad (2)$$

$E_l$  and  $E_m$  are the elastic moduli of layer and matrix respectively. If an elastic layer is embedded in a viscous matrix, the wavelength is given by Biot (1961) as follows:

$$\frac{\lambda_d}{h} = \pi \sqrt[3]{\frac{E_l}{p(1 - \nu_l^2)}} \quad (3)$$

$p$  is the layer parallel-stress and  $\nu_l$  is the poisson's ratio in the stiff layer. Fletcher (1974) developed a folding theory for layers with non-linear rheology where  $n$  represents the power-law-exponent; according to Fletcher (1974) the dominant wavelength is estimated as follows (Fletcher, 1974):

$$\lambda_d/h = 2\pi \left( \frac{\mu_l/\mu_m}{6n} \right)^{1/3} \quad (4)$$

In the early stage of folding, the strain is accommodated by layer thickening and buckling simultaneously. The amplification velocity of the fold is controlled by the kinematic velocity when the folded layer and the matrix show the same material properties (Biot, 1965). In the case where the layer and the matrix exhibit different material properties, the kinematic velocity exists simultaneously with the dynamic velocity (Schmalholz and Podladchikov, 2001). The dynamic velocity is a linear function of the amplitude; hence it grows faster than the kinematic velocity which is a linear function of the thickness of the folded layer. The nucleation amplitude ( $A_N$ ) is the amplitude at which the kinematic velocity is equal to the dynamic velocity. The equation of  $A_N$  is as follows:

$$A_N = \frac{\pi^2}{2} \frac{1}{n} \left( \frac{h}{\lambda_d} \right)^2 \quad (4)$$

Eq. (4) shows that the nucleation amplitude ( $A_N$ ) is a function of the thickness ( $h$ ) and the dominant wavelength. The different formulas of the dominant wavelength mentioned above become invalid at certain amplitudes called the crossover amplitude ( $A_c$ ). The  $A_c$  is expressed as follows (Schmalholz and Podladchikov, 2000):

$$A_c = \frac{A}{\lambda} \approx \frac{1}{\pi} \frac{1}{\sqrt{2\alpha}} \quad (5)$$

Where  $\alpha$ ,  $A$   $\lambda$  are respectively, the fold wavelength, fold amplitude and the general growth rate.



## 4.2 Strain Contour Map

The Strain Contour Map is a new method for estimating strain and viscosity ratios from fold geometry developed by Schmalholz and Podladchikov's (2001); The authors divide the folding process of a fold into three stages (Fig4.2) which are the kinematic thickening, the exponential growth and layer length controlled growth. The kinematic thickening begins when a layer is subjected to layer parallel shortening and finishes when the fold reaches the nucleation amplitude. The nucleation amplitude is the amplitude where the kinematic velocity and dynamic velocity. The kinematic velocity is the amplification velocity of the top boundary of the layer which experiences the deformation (folding)

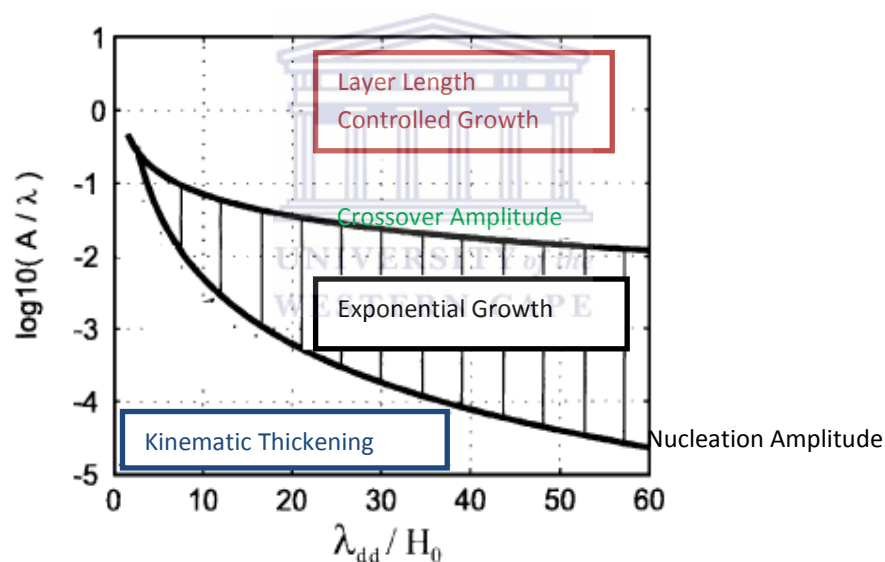


Fig.4.2. Different stages of folding (Schmalholz and Podladchikov, 2000).

When the material properties (mechanical properties) of the layer are different from those of the matrix the dynamic velocity coexist with the kinematic velocity until they become equalled at the nucleation amplitude. At the nucleation amplitude the fold grows exponentially until they reached the crossover amplitude where the fold is controlled by the layer resistance to stretching. The strain estimated using the strain contour map is the strain

accommodate from the nucleation amplitude (Schmalholz and Podladchikov, 2000). Hence the strain accommodated before fold amplification is not taking into account.

The natural strain is defined by:

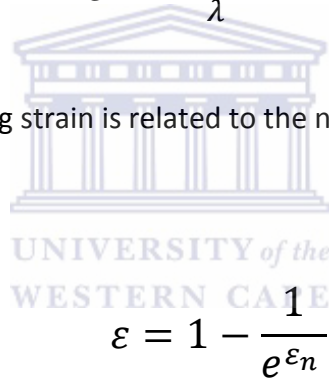
$$\varepsilon_n = \ln\left(\frac{\lambda_0}{\lambda}\right) \quad (6)$$

$\lambda_0$  is the initial wavelength.

The engineering stress (  $\varepsilon$  ) is defined by

$$\varepsilon = \frac{\lambda_0 - \lambda}{\lambda} \quad (7)$$

The engineering strain is related to the natural strain by:



UNIVERSITY of the  
WESTERN CAPE

$$\varepsilon = 1 - \frac{1}{e^{\varepsilon_n}} \quad (8)$$

The natural strain (  $\varepsilon_n$  ) is given by Schmalholz and Podladchikov (2000) as follows:

$$\varepsilon_n = \ln\left(\frac{L_{arc}}{L_{arc0}} \frac{\lambda_0}{\lambda}\right)^{\alpha/(2+\alpha)} + \ln\left(\frac{A}{A_0} \frac{\lambda_0}{\lambda}\right)^{1/(2+\alpha)} \quad (9)$$

$$\alpha = \frac{n}{\pi^2} \left(\frac{\lambda_d}{h}\right)^2 \quad (12)$$

$L_{arc}$  and  $\alpha$  are the initial arc length of the folded layer and the general growth rate respectively. The first order of Taylor's equation of Eq. (9) for  $\alpha \gg 1$  gives:

(11)

$$\varepsilon_n = \ln \left( \frac{L_{arc}}{L_{arc0}} \frac{\lambda_0}{\lambda} \right)$$

The arc length of a layer with initial sinusoidal shape can be approximated as follows (Schmalholz and Podladchikov, 2000):

$$\frac{L_{arc}}{\lambda} = 1 + \frac{\pi^2 (A/\lambda)^2}{1 + 3(A/\lambda)^2}$$

By substituting Eq. (11) in Eq. (12) and assuming that  $\frac{\lambda_0}{L_{arc0}} \approx 1$  and replacing engineering strain by natural strain, yields the following formula:

$$\frac{A}{\lambda} = \frac{\sqrt{\varepsilon}}{\sqrt{\pi^2(1 - \varepsilon) - 3\varepsilon}} \quad (13)$$

By substituting Eqs. (11) and (12) in Eq. 9; assuming that  $\frac{\lambda_0}{L_{arc0}} \approx 1$  and  $n=1$ , Eq. 9 becomes:

$$\varepsilon_n = \ln \left( 1 + \frac{\pi^2 (A/\lambda)^2}{1 + 3(A/\lambda)^2} \right)^{\frac{1}{\pi^2 \left( \frac{\lambda_d}{h} \right)^2 / \left( 2 + \frac{1}{\pi^2} \left( \frac{\lambda_d}{h} \right)^2 \right)}} + \ln \left( \frac{A}{A_0} \frac{\lambda_0}{\lambda} \right)^{1 / \left( 2 + \frac{1}{\pi^2} \left( \frac{\lambda_d}{h} \right)^2 \right)} \quad (14)$$

Eq.14 shows that the natural strain depends on two geometric ratios:  $A/\lambda$  and  $\lambda_d/h$ . The strain contour map is constructed by plotting amplitude/wavelength ( $A/\lambda$ ) against thickness / wavelength ( $\lambda/h$ ). The strain contour map is divided into bold lines called folding lines. A folding line is the characteristic line containing all points that are defined at different strains, the measured ( $A_N/\lambda_d$ ) and ( $\lambda_d/h$ ) values for a fixed viscosity ratio; the

initial point of a folding line corresponds to the initial dominant wavelength and the nucleation amplitude ( $A_N$ ). For correction purposes  $A/\lambda$  is replaced in Eq.12 by  $(A/\lambda) - C_1 h/\lambda$ ,  $C_1$ , where  $C_1$  is the average slope of the strain contour because all strain contours display a negative slope with increasing  $h$ . The folding line of viscosity contrast 50 defines the boundary where the strain contour slope  $C_1$  changes to  $C_2$ . This folding line is approximated as follows:

$$A/\lambda \approx -0.22 + 2.43 \frac{h}{\lambda} \quad (15)$$

The strain contour line (blue line) is then constructed by solving Eq. (14) for strain and correcting  $A/\lambda$  by the slopes  $C_1$  and  $C_2$ , we obtain:

$$\varepsilon = \frac{\pi^2 (A/\lambda)^2}{1 + (A/\lambda)^2 (\pi^2 + 3)} \quad (16)$$

After correcting  $A/\lambda$  for the slopes  $C_1$  and  $C_2$ , this yields:

$$\varepsilon = \frac{\pi^2 Z^2}{1 + Z^2 (\pi^2 + 3)} \quad (17)$$

With

$$Z = \begin{cases} A/\lambda + C_1 H/\lambda & \text{if } H/\lambda < H_{50} \\ A/\lambda + C_2 H/\lambda + (C_1 - C_2)H_{50} & \text{if } H/\lambda > H_{50} \end{cases} \quad (18)$$

$$H_{50} = (A/\lambda + 0.22) / 2.43, \quad C_1 = 0.8, \quad C_2 = 0.4$$

### 4.3 Results and Interpretations

The estimation of shortening and competence contrast in our study is done using four shape parameters; the arclength (L), amplitude (A), the wavelength ( $\lambda$ ) and thickness (h). Fold Geometry Toolbox (Adamuszek et al., 2011), an open source MATLAB application allows an accurate and rapid calculation of fold geometric parameters.

Table 4.1. Fold shape parameters (multiplied by 1000)

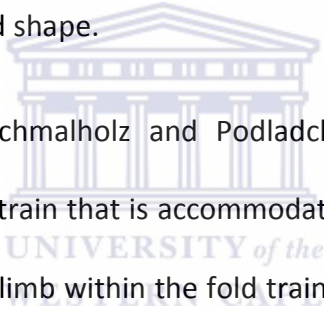
Parameters(mm)	Fold 1		Fold 4		Fold 6		Fold 7		Fold 11	
	upper	lower	upper	lower	upper	lower	upper	lower	upper	lower
<b>Av.Amplitude</b>	62.4	65.4	34.8	38.7	29.3	40.9	66.4	62.9	77.3	75.3
<b>Av.Wavelength</b>	241	189	378	423	335	403	57	733	348	34
<b>Av.Thickness</b>	33.2	33.2	38.7	38.7	43.1	43.1	156	156	120	120
<b>Viscosity Ratio(VRSC)</b>	40.1		31.7		8.4		2		1.7	
<b>VRFS</b>	~ 53		~37		-		-		-	
<b>Stretch %</b>	~ 85		~92		-		-		-	
<b>VRSP</b>	~100	~80	~75	~75	~35	~35	~25	~12.5	~20	~20
<b>Bulk shortening%</b>	~48	~60	~20	~20	~28	~28	~30	~40	~53	~53

Fold shape parameters (multiplied by 1000) used to estimate the viscosity ratio and the shortening. The parameters are evaluated for upper and lower fold interfaces. The viscosity ratio is calculated using various methods. VRSC represents viscosity ratio obtained from Sherwin and Chapple (1968) model. VRFS is the viscosity ratio obtained from Fletcher and Sherwin graph (1978). VRSP represent the viscosity ratio obtained from the strain contour map (Schmalholz and Podladchikov, 2001).

Viscosity ratio and shortening are estimated by the Fold Geometry Toolbox (FGT) using various numerical and analytical methods. Natural folds (Fig 4.6) of metre scale that formed during the second phase of deformation of the Warm Zand Structure were digitized in Adobe Illustrator and exported in FGT. Table 4.1 displays the results of the numerical analysis of the natural folds mentioned above. The amplitude of folds is calculated using the definition of Ramsey and Huber (1987). The variability of the amplitude values of the upper and lower interfaces are very small for Fold 1, Fold 4, Fold 7 and Fold 11; however the data spans are larger for amplitude values of the upper and lower interface of Fold 6; this might be due to errors introduced during the digitization process. The value for amplitude, wavelength and thickness are used to estimate the viscosity ratio and shortening. Table 4.1 shows the results of viscosity ratio and shortening analysis. The viscosity contrasts of Fold 6, Fold 7 and Fold 11 using the models of Sherwin and Chapple, 1968; Biot, 1961, 1965; Ramberg, 1961; Currie et al., 1962; Fletcher, 1974, give respectively 8.4, 2, 1.7. The small viscosity contrast values obtained can be explained by the high values of the amplitude of folds under study. Hence the models used to obtain these viscosity values (8.4, 2, 1.7) are only valid for fold with infinitesimal amplitudes. The method by Fletcher and Sherwin (1978) yields a viscosity ratio close to 47 (Fig.4.4a), and indicates that the stretch at which wavelength selection took place is  $\sim 85$ . The strain contour map (Fig.4.4b) shows blue dots which represent individual folds in the fold train. The viscosity ratio and shortening of a single fold train (red point) is obtained by calculating the average of the viscosity ratio and shortening of individual folds in fold train. For Fold 1, in the strain contour map (Fig.4.4b), the amplitude wavelength ratio (11.87) yields an average viscosity ratio and shortening of  $\sim 50$  and  $\sim 70$  for the upper fold interface and of  $\sim 48$  and  $\sim 60$  for lower fold interface. In

Table 4.1, the individual folds, Fold 6, Fold 7 and Fold 11 do not yield any viscosity and shortening values.

Fig.4.6a shows that the red point indicating the shortening and stretch value of Fold 11 is out of range in Fletcher and Sherwin graph (1978). These observations show that the Fletcher and Sherwin graph cannot be used to analyse individual folds, but should rather be used to analyse fold train. Fold 11 analysed by the strain contour map yields a viscosity ratio of  $\sim 20$  and shortening of  $\sim 53$  (Fig.4.5b). Hence Fig.4.5b shows that the strain contour map analyses the individual folds better compared to Fletcher and Sherwin, (1978) method. In the latter case it is important to notice that the blue dots do not represent individual folds, but rather irregularities in the fold shape.



In the field of fold analysis, Schmalholz and Podladchikov (2001) defined the strain partitioning as the difference in strain that is accommodated by the whole fold train on the one hand and the individual fold limb within the fold train on the other hand. Fold 1 (Table 4.2) shows a constant increase of 1% for strain partitioning whereas Fold 9 (Table 4.3) shows an increase of 4%, 5%, 8%, and 10% for the strain partitioning. Numerical modelling (Schmalholz and Podladchikov, 2001) demonstrated that the strong viscoelastic fold trains display a strong increase in strain partitioning while viscous fold strains demonstrate a slight increase in strain. Hence by comparing our results with those of Schmalholz and Podladchikov (2001), we can infer that Fold 9 exhibits a viscoelastic rheology while Fold 1 exhibits a viscous rheology.

In summary the viscosity contrast of the folds collected in the Puntsit Formation in the Warm Zand Structure is between 100-53. The bulk shortening on the other hand is between 60-53%. It important to mention that the evaluation of the bulk shortening using the strain

contour map does not take into account the layer parallel shortening prior to the onset of fold amplification (Schmalholz and Podladchikov, 2001). The values of the shortening found in this study agree with the results found by van Bever Donker (1980). According to van Bever Donker (1980) the shortening in  $D_2$  exceeded 23% but probably did not exceed 60% except for the Neusberg area. However it cannot be said with certitude which kinematic fold mechanisms are responsible of the accommodation of strain these folds or in which order they occur in each fold. The next chapters will deal with numerical modelling of the strain pattern of fold or the order in which the kinematic folding mechanisms occur in the folds in the Warm Zand Structure.





## Linear viscous (Biot, 1961)

$$\frac{l}{h} = 2\pi^3 \sqrt{\frac{\mu_l}{6\mu_m}}$$

$$\frac{\mu_l}{\mu_m} = 40.1$$

## Multilayers viscous (Biot, 1961)

$$\frac{l}{h} = 2\pi^3 \sqrt{\frac{N\mu_l}{6\mu_m}}$$

$$\frac{\mu_l}{\mu_m} = 40.1$$

## Non-linear viscous (Fletcher, 1974)

$$\frac{l}{h} = 2\pi^3 \sqrt{\frac{\mu_l}{6\mu_m} \frac{\sqrt{n_m}}{n_l}}$$

$$\frac{\mu_l}{\mu_m} = 40.1$$

## Linear Elastic (Currie et al, 1962)

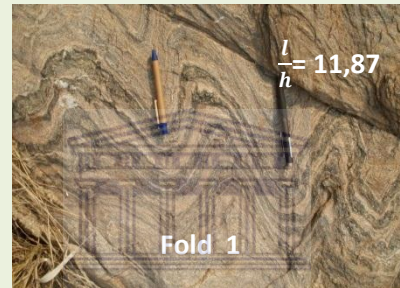
$$\frac{l}{h} = 2\pi^3 \sqrt{\frac{E_l}{6\mu_m}}$$

$$\frac{E_l}{E_m} = 40.1$$

## Visco-elastic (Biot, 1961)

$$\frac{l}{h} = \pi^3 \sqrt{\frac{E_l}{p(1-\nu_l^2)}}$$

$$\frac{E_l}{P} = 13.1$$



## Thickening correction (Sherwin and Chapple, 1968)

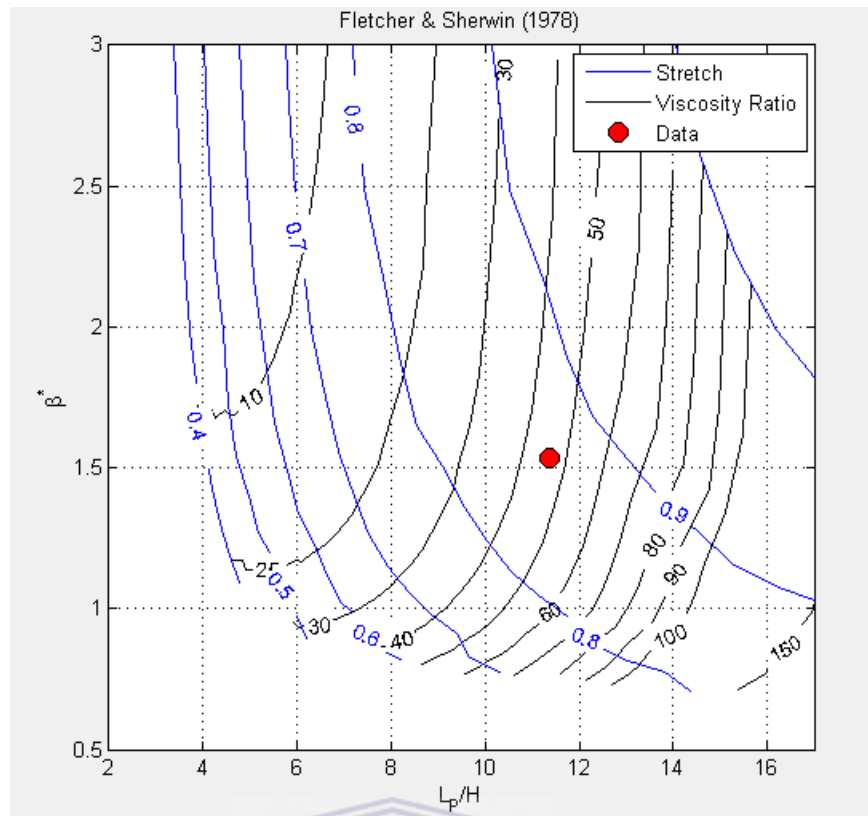
$$\frac{l}{h} = 2\pi^3 \sqrt{\frac{\mu_l}{6\mu_m} \frac{S_x^2 (S_x^2 - 1)}{2}}$$

$$\frac{\mu_l}{\mu_m} = 40.1$$

- $E_l$  - Young's modulus of layer
- $E_m$  - Young's modulus of matrix
- $h$  - Thickness
- $l$  - Arclength
- $\mu_l$  - Viscosity of the layer
- $\mu_m$  - Viscosity of matrix
- $\nu_l$  - Poisson's ratio
- $N$  - Number of layers
- $n_l$  - Power-law of layer
- $n_m$  - Power-law of matrix
- $P$  - Layer parallel stress
- $S_x$  - Layer stretch in x direction

Fig.4.3. Estimation of viscosity contrast of Fold

(a)



(b)

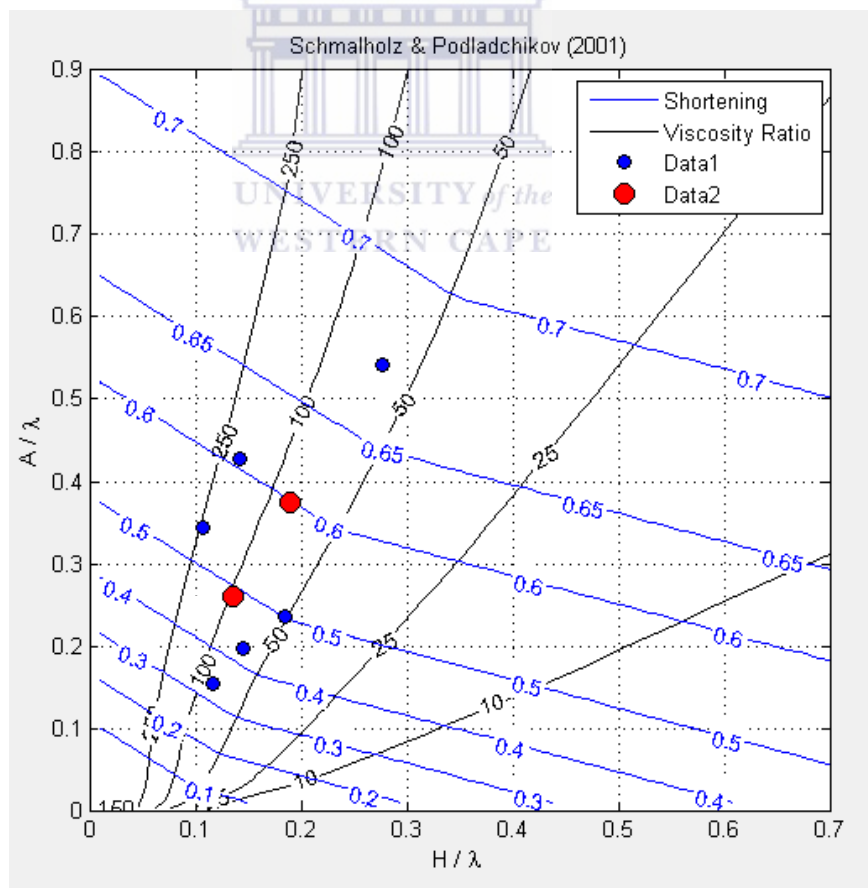


Fig.4.4. Strain of viscosity ratio of Fold 1. (a) Fletcher and Sherwin (1978). (b) Schmalholz and Podladchikov (2001). A- Amplitude, H- Thickness,  $\lambda$  – wavelength,  $\beta^*$  relative band width of amplitude spectrum and  $L_p$  – Preferred wavelength

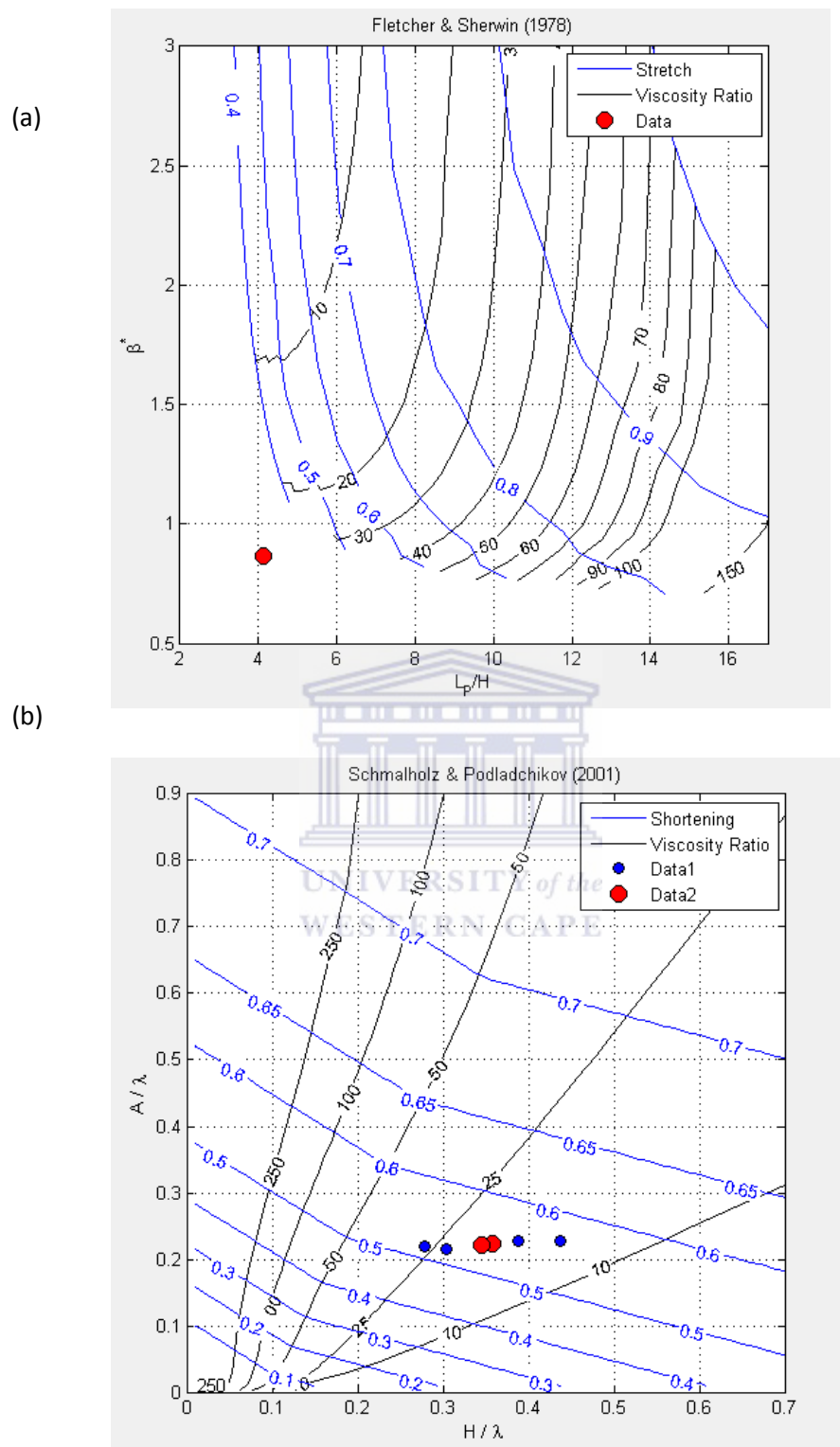
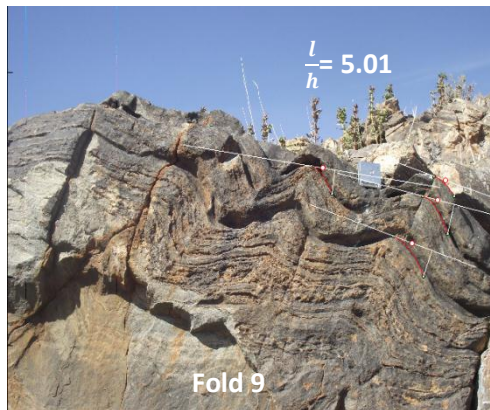
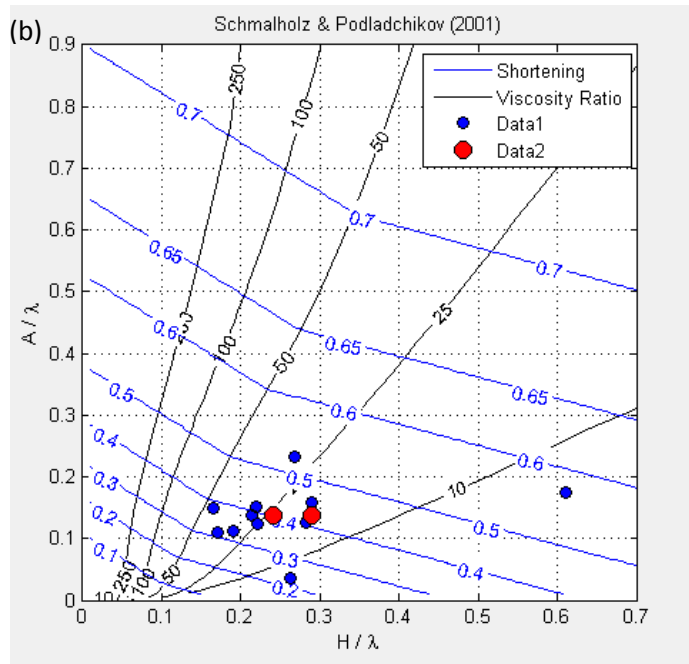


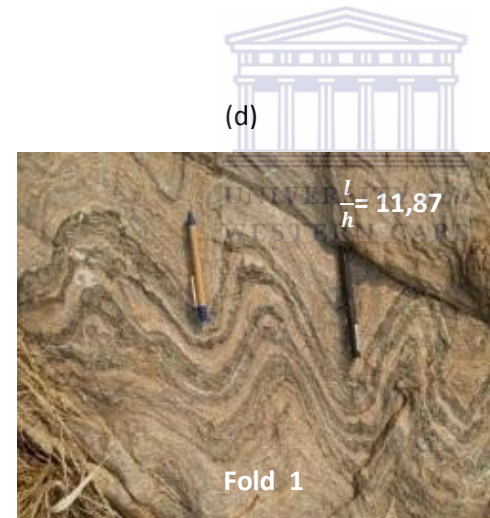
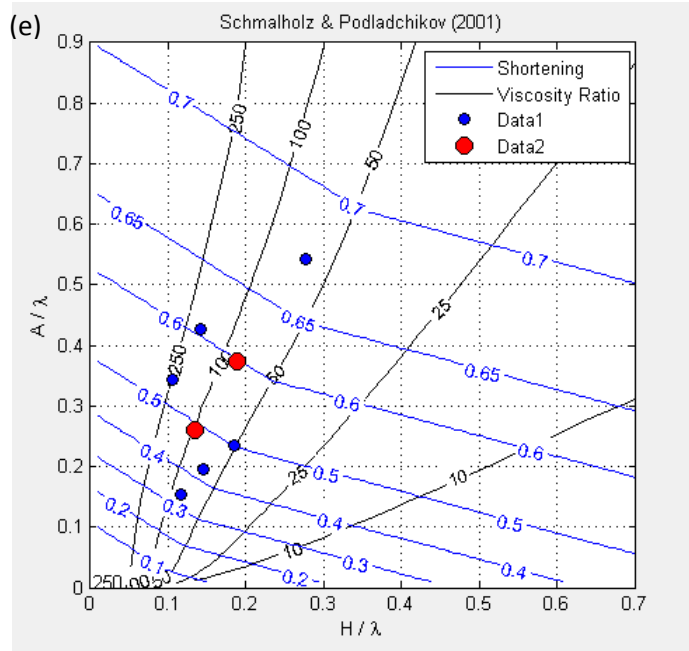
Fig.4.5. Graph of viscosity ratio of Fold 11. (a) Fletcher and Sherwin (1978). (b) Schmalholz and Podladchikov (2001). A- amplitude, H- thickness,  $\lambda$  – wavelength,  $\beta^*$  relative band width of amplitude spectrum and  $L_p$  – preferred wavelength.



(c)

Fold 9 (fold strain)		
Bulk Strain %	Ind. Strain%	Strain Partitioning%
43	40	3
	39	4
	38	5
	37	6
	30	13
	24	19

Table 5.2. Strain partitioning analysis of Fold 9



(f)

Fold 1 (fold strain)		
Bulk Strain %	Ind. Strain%	Strain Partitioning%
60	60	1
	55	5
	50	10
	42	18
	32	28

Table 4.3. Strain partitioning analysis of Fold 1

Fig.4.6. Strain partitioning analysis. (a) Picture of Fold 9. (b) Strain contour map of Fold 9. Blue dots represent individual strain and red dots bulk strain. (c) Table 5.2. Strain partitioning analysis of Fold 9. (d) Picture of Fold 1. (e) Strain contour map of Fold 1. Blue dots represent individual strain and red dots bulk strain. (f) Table 5.3. Strain partitioning analysis of Fold 1.

---

# Chapter 5

---

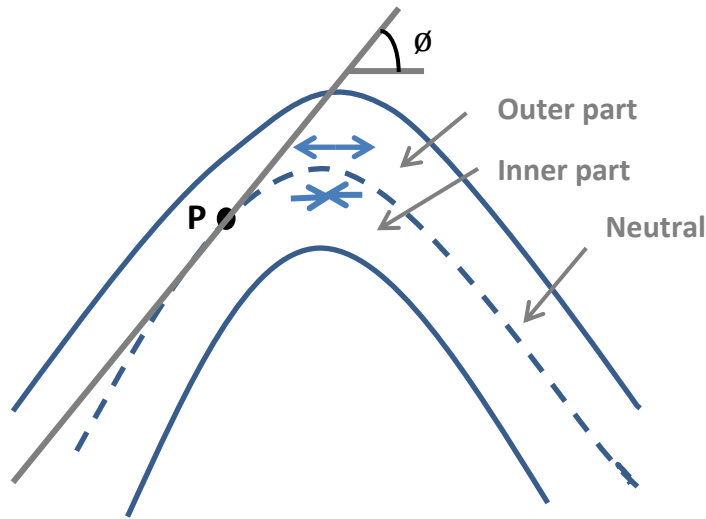
## Parameters Controlling the Geometry of Folds

### 5.1 Introduction

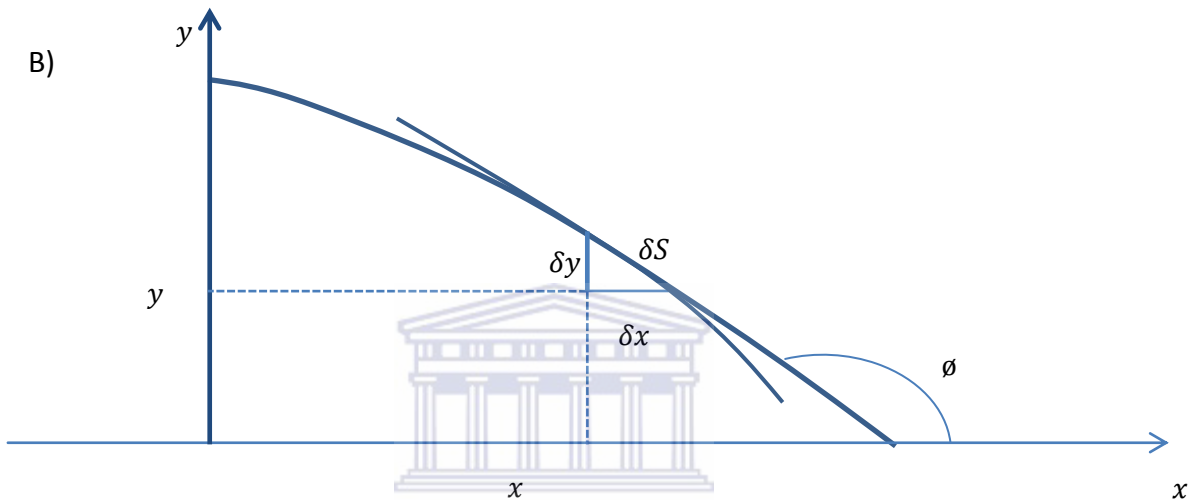
The strain pattern fold is the combination the kinematical folding mechanisms responsible of the accommodation on strain during the folding process. Kinematical folding mechanisms describe the different ways in which folds accommodate the strain. Four kinematic folding mechanisms have been recognized; Initial Layer Shortening (ILHS), Flexural Flow (FF), and Tangential Longitudinal Strain (TLS) and Flattening (FL). Strain patterns are the result of the superposition of kinematic folding mechanisms and are almost impossible to observe in the field; hence the study of the strain pattern requires the use of numerical simulations. Scientific simulations take advantage of numerical methods to calculate an approximate solution of differential equations and are thus referred as numerical simulations.

The first step of numerical modelling in this study will be to determine the parameters that control the geometry of folds; the second step will be the mathematical modelling of each kinematical fold mechanism and the third step will be the simulation of theoretical folds by superposing mathematical model of kinematical fold mechanisms. The theoretical folds that will match the parameters of the natural folds under study would have been simulated with the correct strain pattern which is the correct combination of kinematical folding mechanisms.

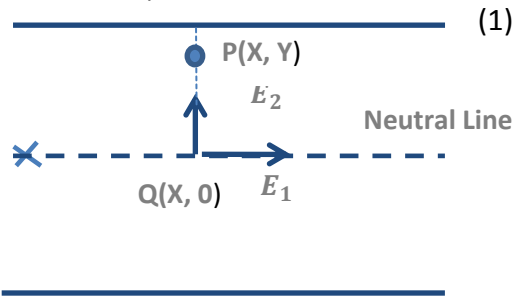
A)



B)



C)



(2)

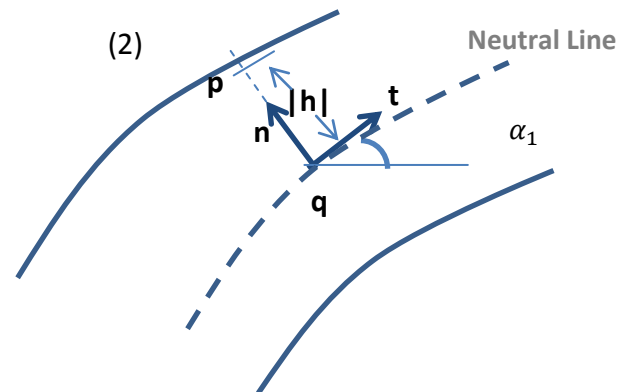


Fig.5.1: A) Tangential longitudinal strain and curvature of the neutral line  $k$  ;  $\phi$  being the angle between the tangent line at P and the positive x-axis; B) Small increment in x and y direction respectively named  $\delta x$  and  $\delta y$ .  $\delta s$  is the hypotenuse of the triangle formed by  $\delta x$  and  $\delta y$  and which is the change in arc-length along the curve; C) Geometrical analysis of the NL after folding. (1) Neutral before folding. (2) Neutral line after folding P and Q are transformed into p and q. (N.C. Bobillo-Ares et al 2000)

To study the parameters that control the geometry of the folds, we are going to analyse a layer deformed by the Tangential Longitudinal Strain (TLS) only. It is worth to stress that this is an ideal situation because in reality folds cannot be the result of only one kinematic folding mechanism as we mentioned earlier. A layer deformed by TLS displays a neutral line, the following mathematical model shows that the neutral line can be modelled using a simple function  $y = f(x)$

## 5.2) Mathematical Analysis of a Layer Folded by TLS

N.C Bobillo-Ares et al (2000) using the deformation analysis found in Truesdell and Toupin (1960) (pp.241-261) and Mase (1970) (pp.91-108), analysed the deformation within a layer folded by tangential longitudinal strain as follow: ( $\mathbf{t}$ ) Is the tangent unit vector, ( $\mathbf{n}$ ) the normal vector, ( $\rho$ ) the curvature radius

$$\left. \begin{aligned} \frac{d\mathbf{t}}{ds} &= -\frac{1}{\rho} \mathbf{n} \\ \frac{d\mathbf{n}}{ds} &= -\frac{1}{\rho} \mathbf{t} \end{aligned} \right\} \quad (20)$$

$X$  the length parameter of the neutral line and  $\psi(X,0)$  representing the neutral line,  $Q(X,0)$  the orthogonal projection of an undeformed point  $P(X,Y)$  on the neutral line (Fig.5.3a). The point  $p = \psi(P)$  located on the normal to neutral line at point  $q = \psi(Q)$  obtained by deformation of Q. The mathematical equation describing the transformation of the initial point P to the deformed P is given by:  $p = \psi(P) = \psi(Q) + h(X,Y)\mathbf{n}(X) = \psi(X,0) + h(X,Y)\mathbf{n}(X)$ .

The partial derivative of  $p$  with respect to undeformed co-ordinates are:

$$\mathbf{F}(\mathbf{E}_1) = \frac{\partial p}{\partial X} = \frac{\partial \psi(X,0)}{\partial X} + \frac{\partial h}{\partial X} \mathbf{n}(X) + h \frac{d\mathbf{n}}{dX} = \mathbf{t}(X) + \frac{\partial h}{\partial X} \mathbf{n}(X) + \frac{h}{\bar{n}} \mathbf{t}(X) \quad (21)$$



$$= \left(1 + \frac{h}{p}\right) \mathbf{t}(X) + \frac{\partial h}{\partial X} \mathbf{n}(X),$$

$$\mathbf{F}(\mathbf{E}_2) = \frac{\partial P}{\partial Y} = \underbrace{\frac{\partial \psi(X,0)}{\partial Y}}_0 + \frac{\partial h}{\partial Y} \mathbf{n}(X)$$

The area conservation condition is:

$$\left(1 + \frac{h(X, Y)}{\rho(X)}\right) \frac{\partial h}{\partial Y}(X, Y) = 1$$

Rearranging, we have:

$$\rho(X) \frac{\partial h}{\partial Y}(X, Y) + h(X, Y) \frac{\partial}{\partial Y} h(X, Y) - \rho(X) = 0$$

The general solution of the Eq.24 is:

$$\rho(X)h(X, Y) + \frac{1}{2}h^2(X, Y) - \rho(X)Y = f(X),$$

Assuming the boundary conditions,  $Y = 0$  and  $h(X, 0) = 0$ , this result in the following equation:

$$h^2(X, Y) + 2\rho(X)h(X, Y) - \rho(X)Y = 0$$

The solution of the quadratic equation Eq.26 is:

$$h(X, Y) = -\rho(X) + \sqrt{\rho^2(X) + 2\rho(X)Y}$$

From this, the author found that:

$$\frac{\partial}{\partial Y} h(X, Y) = \rho'(X) \frac{h^2}{2\rho(h+\rho)} \frac{\partial}{\partial Y} h(X, Y) = \frac{\rho}{\rho+h} \quad (28)$$

According to Eqs.14 and 15 the material deformation gradient at the base ( $\mathbf{t}, \mathbf{n}$ ) is given by the following equation:

$$\mathbf{F} = \begin{bmatrix} \frac{\rho}{\rho + h} & 0 \\ \rho' \frac{h^2}{2\rho(h + \rho)} & \frac{\rho}{\rho + h} \end{bmatrix}$$

The curvature radius is replaced by the curvature since in the points with zero; the radius of curvature is infinite:

$$\mathbf{F} = \begin{bmatrix} 1 + kh & 0 \\ \frac{h^2}{2\rho(1 + kh)dX} & 1 + kh \end{bmatrix}$$

$y = f(x)$  is the function that described the neutral line after folding. In order to found out what functions which best fit the neutral line, we tried to model the latter with Fourier series, conic function, power function, cubic Bezier curves and sub-ellipses and super-ellipses. The parameters obtained from each family of function were used to classify the folds. The family of function that will display the same results as those obtained from the traditional methods of fold classification will be considered as the best match for the neutral line.

### 5.3.1) Fourier Series

The Fourier series of a function with a period  $2\pi$  and integrable between  $-\pi$  and  $\pi$  by:

$$f(x) = \frac{a_0}{2} + \sum_{n=1}^{\infty} (a_n \cos nx + b_n \sin nx)$$

$$\text{With } a_n = \frac{1}{\pi} \int_{-\pi}^{\pi} f(x) \cos nx \, dx, \quad (n = 0, 1, 2, \dots) \quad (32)$$

$$a_n = \frac{1}{\pi} \int_{-\pi}^{\pi} f(x) \sin nx \, dx, \quad (n = 1, 2, \dots) \tag{33}$$

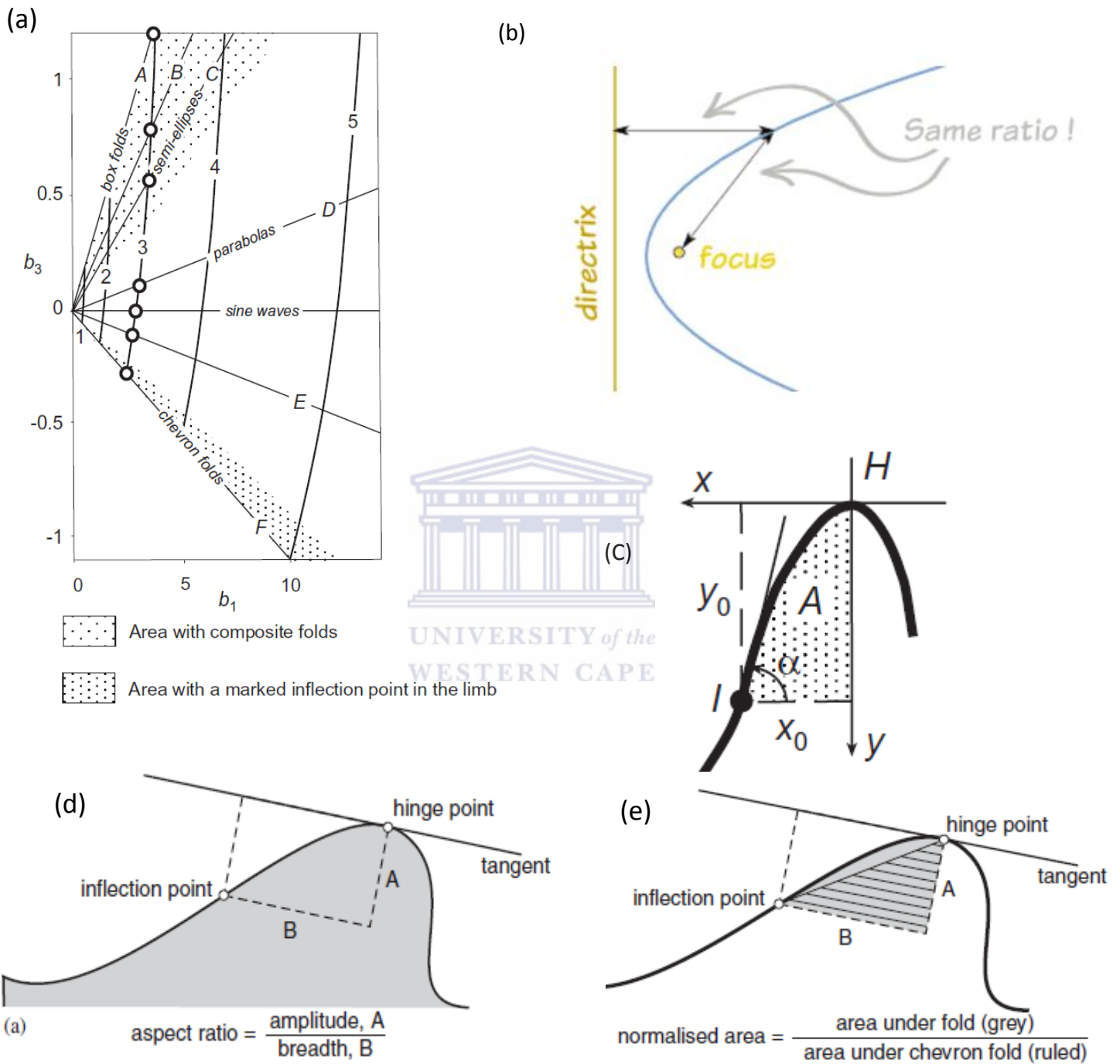
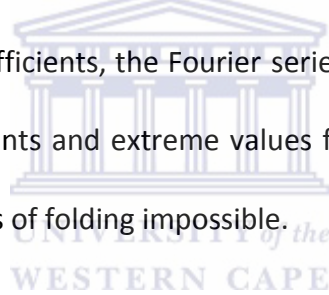


Fig.5.2.(a) Hudleston diagram (1979). (b) Definition of conic section. (c) Fold profile: H, hinge point; I, inflection point; A, area beneath the limb profile;  $\hat{\alpha}$ , maximum dip. (d) Description of the aspect ratio of a fold limb. (e) The description of the normalized of a fold limb. (Lisle et al.,2006)

Hudleston (1973) used only the coefficients  $b_1$  and  $b_3$  of a sine series to characterise the profile of a folded surface and constructed a set of idealised folds (Fig.5.2a) for six different shapes ( $b_3/b_1$ ) and five standard amplitudes (1 to 5). The coefficients  $b_1$  and  $b_3$  are determined by comparison of the fold profile of natural folds with the 30 idealised fold forms. Van Zyl (1981) mapped the single folded layers between the Vaalkoppies and Matjiesriver segment (Upington Geotraverse). Furthermore he used the Fourier series to demonstrate that the mesoscopic folds on the western limb of the Karoo antiform differ in geometry from those on the eastern limb. Gert Claus & Jurgen Schlegel (1991) on the other hand used the Fourier series to demonstrate that the folds of the Kheis Province resulted from the superposition of homogeneous flattening strain. Bastista et al. (2005) showed that by increasing the number of coefficients, the Fourier series can provide a good fit for many folds; however the inflection points and extreme values found within the interval in these fits make the kinematical analysis of folding impossible.



### 5.3.2) Conic Sections

The conic sections have been used by Aller et al. (2004) as a basic method for classifying folds with the goal of studying kinematical folding mechanisms. The equation of the conics is as follows :

$$f(e; x) = \begin{cases} \frac{1 - \sqrt{1 - (1 - e^2)x^2}}{1 - e^2} & 0 \leq e(\text{eccentricity}) \neq 1 \\ \frac{x^2}{2} & e = 1 \end{cases} \quad (34)$$

Conics result from the intersection of a cone with a plane. A cone can be defined using a straight line, a point called directrix and focus (Fig.5.2b).

The ratio made by the distance from the focus to a point on the curve divided by the perpendicular distance from the directrix to that point is called the eccentricity ( $e$ ). For an ellipse the eccentricity ( $e$ ) is less than 1; for a parabola, the eccentricity ( $e$ ) is equalled to 1, for a hyperbola, eccentricity ( $e$ ) is greater than 1. In order to use conic sections to represent a grand number of fold profiles, Aller et al. (2004) added a parameter called the scale factor ( $a$ ) which allows the modelling of a cone with only a sector of a conical curve within a fixed interval  $[0, x_0]$  (Fig.5.2c) . Taking into account the scale factor ( $a$ ) the equation of a cone becomes:

$$f(e, a, x) = af\left(e, \frac{x}{a}\right), \quad \text{for } 0 \leq x \leq x_0 \quad (35)$$

To classify fold profiles, it is necessary to define two parameters, the aspect ratio  $h$  and the normalized area  $\mathbf{A}$  .The aspect ratio (Fig.4.2d) is the ratio between the amplitude and breadth of the fold; it is given by the equation:

$$h = \frac{y_0}{x_0} \quad (36)$$

$$h = \begin{cases} \frac{x_0}{2a} & \text{for parabola } (e = 1) \\ \frac{a}{x_0} \frac{1}{e^2 - 1} \left( 1 - \sqrt{1 - (1 - e^2) \frac{x_0^2}{a^2}} \right) & \text{for ellipses and hyperbola } (e \neq 1) \end{cases} \quad (37)$$





Fig. 5.5. Fold shape of the Punsit formation analysed by Fold Profiler.



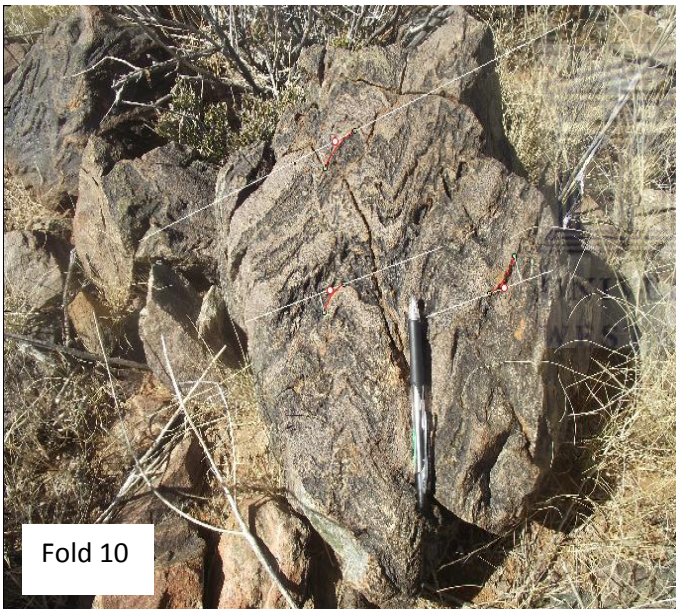
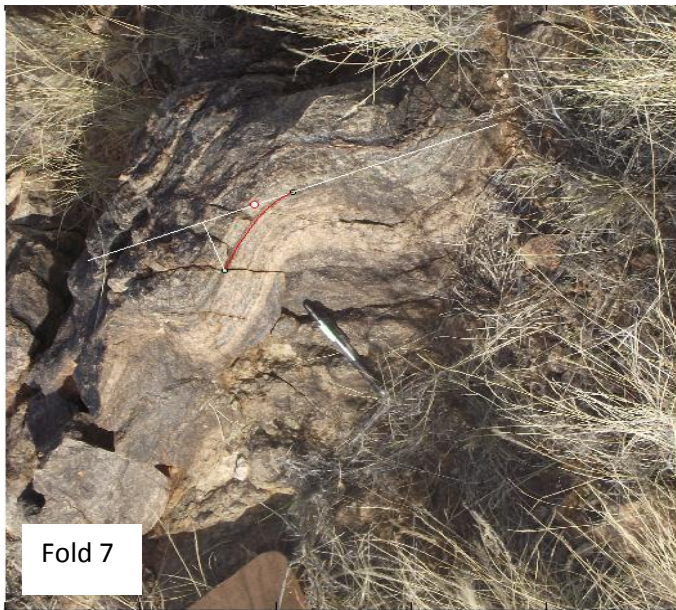


Fig. 5.6. Fold shape of the Punsit formation analysed by Fold Profiler.



The normalized area  $\mathbf{A}$  is an area without physical dimension (Fig.5.2e); it is defined as the area under a fold limb divided by the chevron area of the fold with the same ratio (Lisle et al., 2006). The normalized area  $\mathbf{A}$  is the best parameter to characterize the fold geometry; it is given by the following equation:

$$\mathbf{A} = 2A / x_0 y_0$$

(37)

Where  $A$  is the area enclosed in the concave part within the limb (grey part) interval (Fig.5.2e)

$$\mathbf{A} = 2 - \frac{2}{x_0 f(e, X_0)} \int_0^{X_0} f(e, X) dX$$

(38)

$$\text{With } X_0 = \frac{2h}{1+h^2(1-e^2)}$$

$$\int_0^{X_0} f(e, X) dX = \frac{4}{3} f \text{ for parabolas } (e = 1)$$

(40)

With

$$\int_0^{X_0} f(e, X) dX = \frac{1}{1-e^2} \left[ X_0 - \frac{X_0}{2} \right] \sqrt{1 + (e^2 - 1) X_0^2} - \frac{1}{2\sqrt{e^2-1}} \sin h^{-1} \sqrt{(e^2 - 1) X_0}$$

(41)

For hyperbolas ( $e > 1$ ) and for ellipse

$$\int_0^{X_0} f(e, X) dX = \frac{1}{1-e^2} \left[ X_0 - \frac{X_0}{2} \right] \sqrt{1 - (1 - e^2) X_0^2} - \frac{1}{2\sqrt{1-e^2}} \sin^{-1} \sqrt{(e^2 - 1) X_0}$$

(42)

Fold Profiler (Lisle et al., 2006) is a MATLAB code that allows fold shape classification by comparing fold profile with a mathematical function (Power function, conic sections, bézier curves and sub-ellipses). Fold analysis using Fold Profiler is rapid and allows the theoretical curves to be remodelled during the fitting procedure. The analysis is carried out by uploading the picture of the fold and superimposing the mathematical curves on the digital image of the fold (Fig 5.5). A set of folds of metric scale that formed during the second phase of deformation of the Warm Zand Structure were analysed with Fold Profiler; the folds were named randomly as Fold 1, Fold 2 ...Fold 10 (Fig.5.5 and Fig.5.6). In this study, for each cylindrical folds mentioned early, it is assumed that the section perpendicular to the fold axis is the principal plan, hence the strain analysis using fold shape is considered as a problem of plan strain.

The results of the fold shape analysis using conic sections were displayed as a table (Table 5.1) showing values of the shape parameter  $e$  (eccentricity) aspect ratio and the normalized area of different fold limbs (Fold 1-10). In addition, the results are also displayed as graphs which allow the classification of folds into different shapes. The graphs plot the aspect ratio against the shape parameter  $e$  and the normalized area against the parameter  $e$ .

### 5.3.2) Power Functions

Bastisda et al. (1999) studied the power function of the form,

$$y = y_0 \left( \frac{x}{x_0} \right)^n [0, x_0] \quad (43)$$

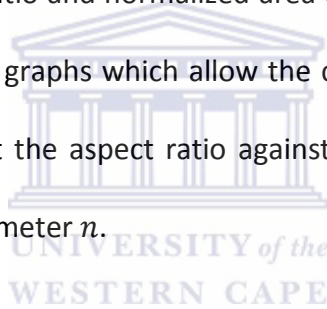
$y_0$  and  $x_0$  are defined in Fig.5.2c.

With the aim of classifying fold and decipher the geometry of fold profile by two parameters, the aspect ratio ( $h = y_0/x_0$ ) and the shape parameter  $n$ , Eq. 43 is changed into:

$$y = y_0 \left( \frac{|x|}{x_0} \right)^n [-x_0, x_0] \quad (44)$$

For cusped folds,  $n > 1$ ; for chevron folds  $n = 1$ ; for sinusoidal folds  $\approx 1.75$ , and for  $n = 2$  parabolic folds. The same set of folds (Fig.5.5 and Fig.5.6) used for the conic methods of classification is used for the power function classification methods.

The results of the fold shape analysis were displayed as a table (Table 5.2) showing values of the shape parameter  $n$ , aspect ratio and normalized area of different fold limbs (Fold 1-10). The results are also displayed as graphs which allow the classification of fold into different shapes. The graphs (Fig.5.8) plot the aspect ratio against the shape parameter  $n$  and the normalized area against the parameter  $n$ .



### 5.3.3) Sub-ellipses and Super-ellipses

The sub-ellipses and super-ellipses concept was used by Lisle (1988) to estimate of shape of coarse clastic sediment particles. Bastida et al. (1999) used the super-ellipses and sub-ellipses concept to fit fold profiles. This family of functions is defined by:

$$\frac{x^p}{x_0^p} + \frac{(y-y_0)^p}{y_0^p} = 1 \quad (45)$$

Eq.(45) describes an ellipse for  $p=2$ ; sub-ellipses for  $p < 2$ ; super-ellipse for  $p > 2$ ; cusped fold for  $p < 1$ , chevron fold for  $p=1$ . The same set of folds (Fig.5.5 and Fig.5.6) is used for the sub-ellipses and super-ellipses classification methods;

Table 5.3 shows the values of fold parameters. The graphs (Fig 5.9) plot the aspect ratio against the shape parameter  $p$  and the normalized area against the parameter  $p$ .

#### 5.3.4. Cubic Bézier Curves

Bézier curves were introduced by a French engineer called Bézier of the automobile industry. A Bézier curve consists of one or more polynomial segments. Each segment is defined by four control points involving eight variables ( $P_0(x_0)$ ,  $P_1(x_1)$ ,  $P_2(x_2)$ ,  $P_3(x_3)$ ). The following parametric equations describe Bézier curves (De Paor, 1996):

$$x(t) = (1-t)^3x_0 + 3(1-t)^2tx_1 + 3(1-t)t^2x_2 + t^3x_3 \quad (46)$$

$$y(t) = (1-t)^3y_0 + 3(1-t)^2ty_1 + 3(1-t)t^2y_2 + t^3y_3 \quad (47)$$

Srivastava and Lisle (2004) introduced constraints that allowed them to define each segment by three points ( $P_0(0, h)$ ,  $P_1(L, h)$ ,  $P_2(1, 0)$ ) and reduced the eight variables to two variables which are the shape parameter ( $L$ ) and the aspect ratio. The resulted simplified parametric equations are as follows:

$$x(t) = 3(1-t)^2tL + 3(1-t)t^2 + t^3 \quad (48)$$

$$y(t) = h [(1-t)^3 + 3(1-t)^2t] \quad (49)$$

Fold classification can be obtained by plotting the aspect ratio  $h$  versus the shape parameter ( $L$ ).

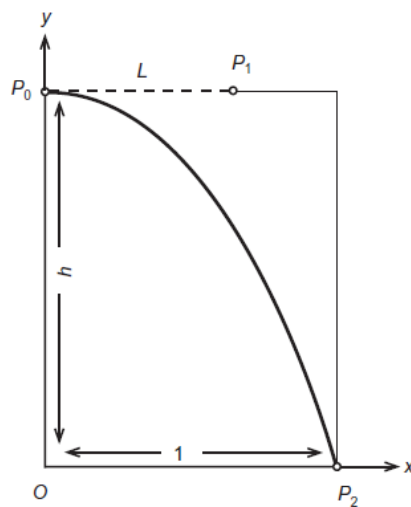


Fig. 5.7. Simplified Cubic Bézier curve used to analyse fold shapes (after Srivastava and Lisle, 2004.)

## 4.4 Results and Interpretations

In this section, we are going to use the word “Fold” with capital F to refer to a picture of folds taken during field work. Some of those pictures contain several single folded layers occurring in the same rocks, for instance Fold 1, Fold 9, and Fold 10 in Fig. 4.5 and Fig. 4.6. Fold limbs on the other hand will be referred to as  $f_{1l_1}$ ,  $f_{1l_2}$ ...  $f_{10l_1}$ . It is noteworthy to notice that for each single folded layer only one fold limb is analysed.

### 4.4.1) Conic Sections

As mentioned earlier the analysis of the shape fold using a conic section involves 3 shape parameters: the eccentricity ( $e$ ), normalized area ( $a$ ), and the aspect ratio ( $R$ ). The results of the analysis of the set of 10 folds from Warm Zand Structure, using the conic section method, are presented in Table 5.1. In Table 5.1, fold limbs ( $f_{1l_1}$ ,  $f_{2l_1}$ ...  $f_{10l_1}$ ) display different values of the shape parameters ( $e$ ,  $a$ ,  $R$ ) for each Fold (Fold 1, Fold 2 ...Fold 10).

For instance in Fold 1, the limb  $f_{1l_1}$  ( $e = 1.001$ ),  $f_{1l_2}$  ( $e = 1.1725$ ),  $f_{1l_3}$  ( $e = 0.8919$ ), and  $f_{1l_4}$  ( $e = 0.7083$ ) display different values of the shape parameter  $e$  which might be interpreted as an

evolution of fold shape in Fold 1. The graph of the aspect ratio versus the eccentricity (Fig.5.8a), shows that Warm Zand Structure fold shape profiles range from ellipse to hyperbola; in addition, the graph of the aspect ratio versus the normalized area (Fig.5.8b) provides more details on the shape of folds by showing that the majority of fold shapes analysed falls between the chevron and parabolic shape. This conclusion is in harmony with the observations made in the field. It is relevant to notice that Fold 6 does not display a chevron shape as it shows in Fig.5.8b

#### 4.4.2) Power Function

The shape parameters obtained from the power function method are displayed in Table 5.2. As we observed with the conic method, the set of folds analysed with the power method, except for Fold 6 and Fold 7, show fold limbs which display different values for each fold shape parameter. In addition, the graph of the aspect ratio versus the shape parameter  $n$  and the graph of aspect ratio versus the normalized area (Fig.5.9b), show different pattern compared to the one observed in the conic functions. It shows that the Warm Zand Structure fold shape profiles display a chevron shape. However Fold 1, Fold 2, Fold 4 and Fold 5 are not chevron folds, hence the power functions parameters cannot be used for our numerical model because they misrepresent the shape of the folds under interest.

#### 4.4.3) Sub-ellipses and Super-ellipses & Bézier curves

The shape parameters obtained from the Sub-ellipses and Super-ellipses method are displayed in Table 5.3. The aspect ratio versus the normalized area graph of the Sub-ellipses and Super-ellipses method display the chevron shape observed in Fold 10 and Fold 9 however it also shows that Fold 4, Fold 5 and Fold 6 are chevron folds which contradict the observations made in the field. The analyse of fold profiles made with the Bézier curves

method (Fig5.10b) displays the same pattern as the analyses made with the conic function. The bézier curves method (Fig5.11a) permits the calculation of the interlimb angles and classify the fold according to their interlimb angle (Fleuty, 1964). According to the interlimb (ILA) angle classification, the majority of fold shapes analysed are concentrated between  $30 < ILA < 70$  (close fold) and  $70 < ILA < 30$  (open fold), this result is in harmony with the observation made in the field. The observations made above clearly demonstrate that the parameters of sub-ellipses and super-ellipses function and the bézier curves cannot be used for our numerical modelling because they misrepresent the geometry of folds of the area of study.

Contrary to the power functions, the sub-ellipses and super-ellipses and the bézier curves the conic functions classification of fold shape is in harmony with the shapes display by the natural folds mapped in the Warm Zand Structure. Therefore the parameters that will be used as input data for our numerical model will be the aspect ratio (R) and the eccentricity (e). These two parameters control the geometry of the fold when the neutral line is modelled using conic functions.



Table 5.1. Fold shape parameter obtained from Fold Profiler® using the conic section

	Fold 1						Fold 2			Fold 3		Fold 4
Fold Limb (fl)	$f_{1 2}$	$f_{1 2}$	$f_{1 2}$	$f_{1 4}$	$f_{1 5}$	$f_{1 6}$	$f_{2 1}$	$f_{2 2}$	$f_{2 3}$	$f_{3 1}$	$f_{3 2}$	$f_{4 1}$
Shape Parameter(e)	1.0001	1.1725	0.8919	0.7083	0.2950	1.0001	1.2797	1.0001	1.0178	0.7961	0.9267	1.8875
Normalised area (a)	1.3333	1.2836	1.3627	1.3826	1.5491	1.3333	1.1979	1.3333	1.3210	1.3916	1.4008	1.2819
Aspect ratio (R)	0.6405	0.6959	0.7396	0.6168	0.9928	0.5937	0.8585	0.7626	1.1301	0.7843	1.3627	0.2705

	Fold 5			Fold 6	Fold 7	Fold 8		Fold 9			Fold 10	
Fold Limb (fl)	$f_{5 1}$	$f_{5 2}$	$f_{5 3}$	$f_{6 1}$	$f_{7 1}$	$f_{8 1}$	$f_{8 2}$	$f_{9 1}$	$f_{9 2}$	$f_{9 3}$	$f_{10 1}$	$f_{10 2}$
Shape Parameter(e)	1.1381	1.1479	1.2445	1.3801	1.3512	1.0661	1.1386	1.1026	1.2758	1.1922	1.2809	1.0001
Normalised area (a)	1.0477	1.2937	1.2693	1.2976	1.2000	1.2782	1.2719	1.2768	1.2751	1.3136	1.2216	1.3333
Aspect ratio (R)	1.7396	0.6767	0.6546	0.3987	0.4939	1.2116	0.8667	0.9761	0.5804	0.4164	0.7835	0.5407

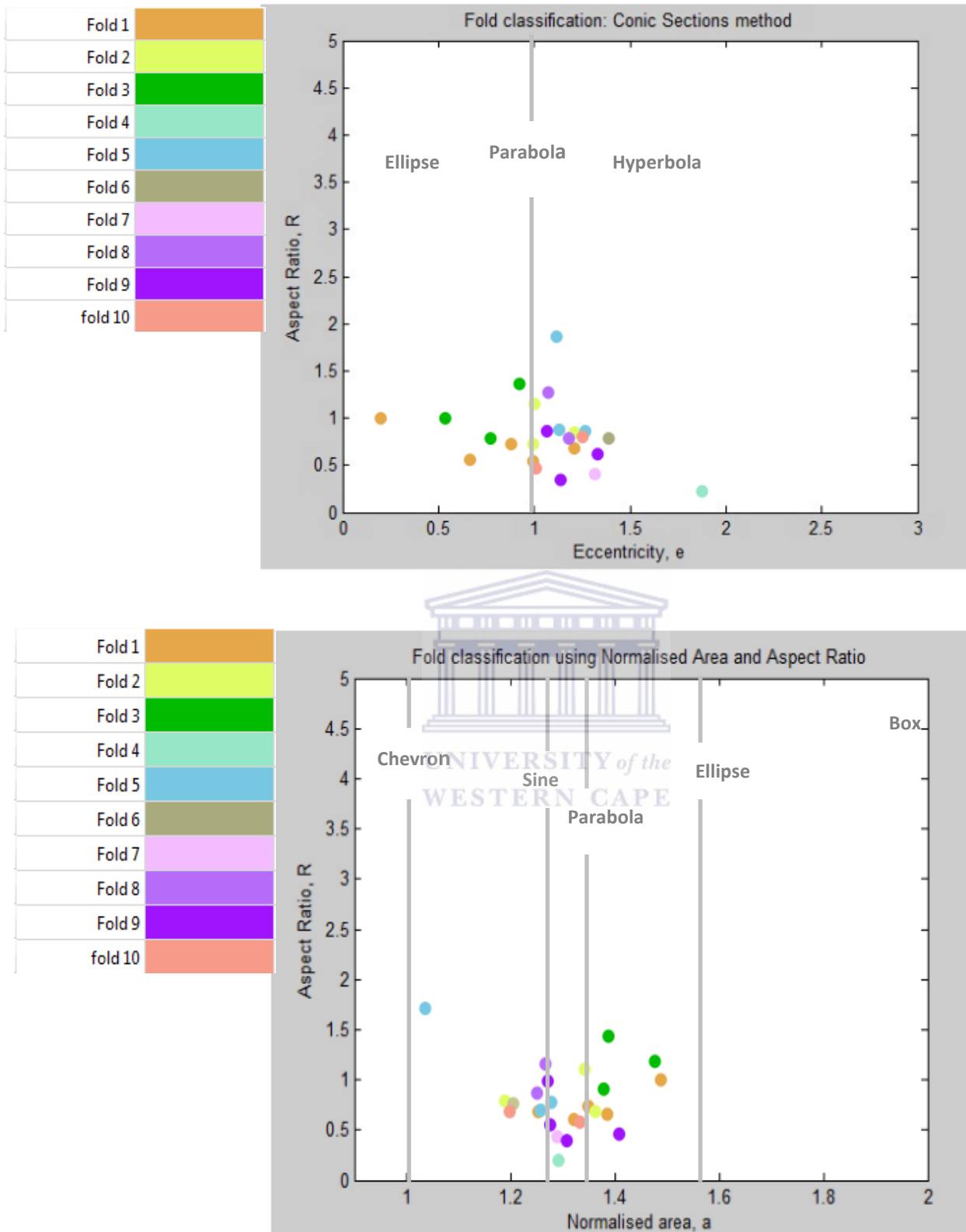


Fig. 5.8. Analysis of the Fold 1-10 using conic section method. (a) Graph of The aspect ratio versus the eccentricity ( $e$ ); (b) graph of the aspect ratio versus the normalised area.

Table 5.2. Fold Shape parameter obtained from Fold Profiler using Power function method

Fold 1							Fold 2				Fold 3	Fold 4
Fold Limb (fl)	$f_{1 2}$	$f_{1 2}$	$f_{1 2}$	$f_{1 4}$	$f_{1 5}$	$f_{1 6}$	$f_{1 7}$	$f_{2 1}$	$f_{2 2}$	$f_{2 3}$	$f_{3 1}$	$f_{4 1}$
Shape Parameter (n)	1.4000	1.4000	2.3000	2.1000	2.4000	1.8000	0.8000	1.4000	1.9000	1.1000	1.8000	1.5000
Normalised area (a)	1.1667	1.1667	1.3939	1.3548	1.4118	1.2857	0.8889	1.1667	1.3103	1.0476	1.2857	1.2000
Aspect ratio (R)	1.2093	0.4984	0.7666	0.5810	0.5088	0.8339	0.2281	0.9479	0.9873	0.6323	0.7881	0.4074

Fold 5			Fold 6	Fold 7	Fold 8	Fold 9	Fold 10					
Fold Limb (fl)	$f_{5 1}$	$f_{5 2}$	$f_{5 3}$	$f_{6 1}$	$f_{7 1}$	$f_{8 1}$	$f_{9 1}$	$f_{9 2}$	$f_{9 3}$	$f_{9 4}$	$f_{10 1}$	$f_{10 2}$
Shape Parameter(n)	1.0000	1.5000	1.2000	1.4000	1.5000	1.3000	2.0000	1.6000	1.5000	2.1000	0.8000	1.3000
Normalised area (a)	1.0000	1.2000	1.0909	1.1667	1.2000	1.1304	1.3333	1.2308	1.2000	1.3548	0.8889	1.1304
Aspect ratio (R)	0.6942	0.5269	0.7203	0.7268	0.4939	3.6875	0.7620	0.7450	0.4863	0.3258	0.4080	0.7933

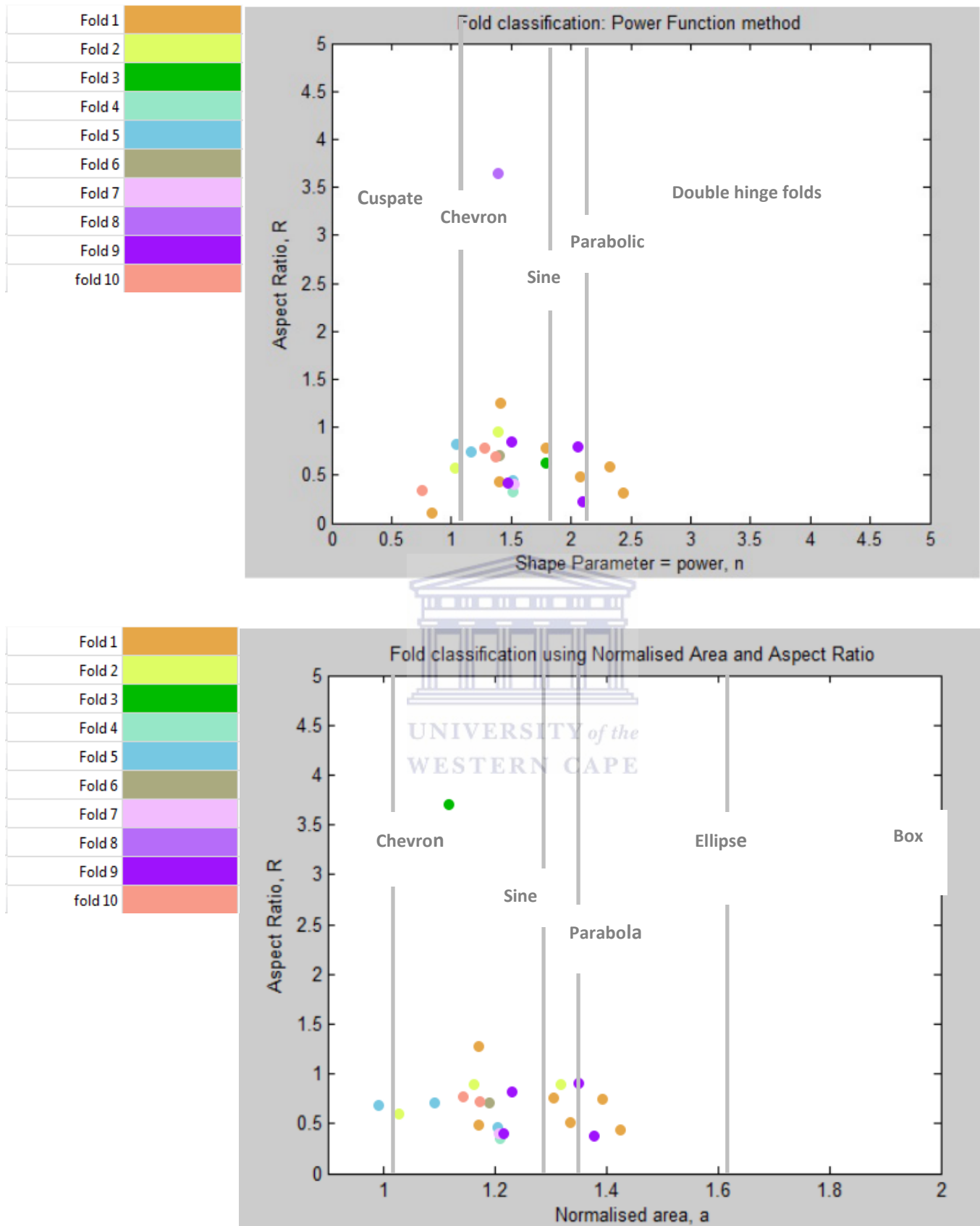


Fig. 5.9. Analysis of the Folds 1-10 using power functions method. (a) Graph of the aspect ratio versus the shape parameter  $n$ ; (b) graph of the aspect ratio versus the normalised area.

Table 5.3 Fold shape parameters obtained using Ébiezer curve method

Fold 1							Fold 2			Fold 3		Fold 4
Fold Limb (fl)	$f_{1 2}$	$f_{1 2}$	$f_{1 2}$	$f_{1 4}$	$f_{1 5}$	$f_{1 6}$	$f_{2 1}$	$f_{2 2}$	$f_{2 3}$	$f_{3 1}$	$f_{3 2}$	$f_{4 1}$
Shape Parameter (P)	1.2000	1.5000	1.3000	1.5000	1.5000	1.5000	1.2797	1.0001	1.0178	1.6000	1.7000	1.0000
Normalised area (a)	1.1762	1.3689	1.2486	1.3689	1.3689	1.3689	1.1979	1.3333	1.3210	1.4189	1.4634	1.0000
Aspect ratio (R)	1.3381	0.8702	0.6487	0.5666	0.5666	0.4425	0.8585	0.7626	1.1301	1.0742	0.7866	0.4762

Fold 5			Fold 6	Fold 7	Fold 8	Fold 9			Fold 10			
Fold Limb (fl)	$f_{5 1}$	$f_{5 2}$	$f_{5 3}$	$f_{6 1}$	$f_{7 1}$	$f_{8 1}$	$f_{9 1}$	$f_{9 2}$	$f_{9 3}$	$f_{9 4}$	$f_{10 1}$	$f_{10 2}$
Shape Parameter (P)	1.0000	1.0000	1.3000	1.3000	1.2000	1.3000	1.3000	1.2000	1.3000	1.4000	1.0000	1.2000
Normalised area (a)	1.0000	1.0000	1.2486	1.2486	1.1762	1.1304	1.2486	1.1762	1.2486	1.3125	1.0000	1.1762
Aspect ratio (R)	0.6437	0.8360	1.0004	1.0336	0.6922	3.6875	0.6378	0.6982	0.6943	0.5667	1.5579	1.9530

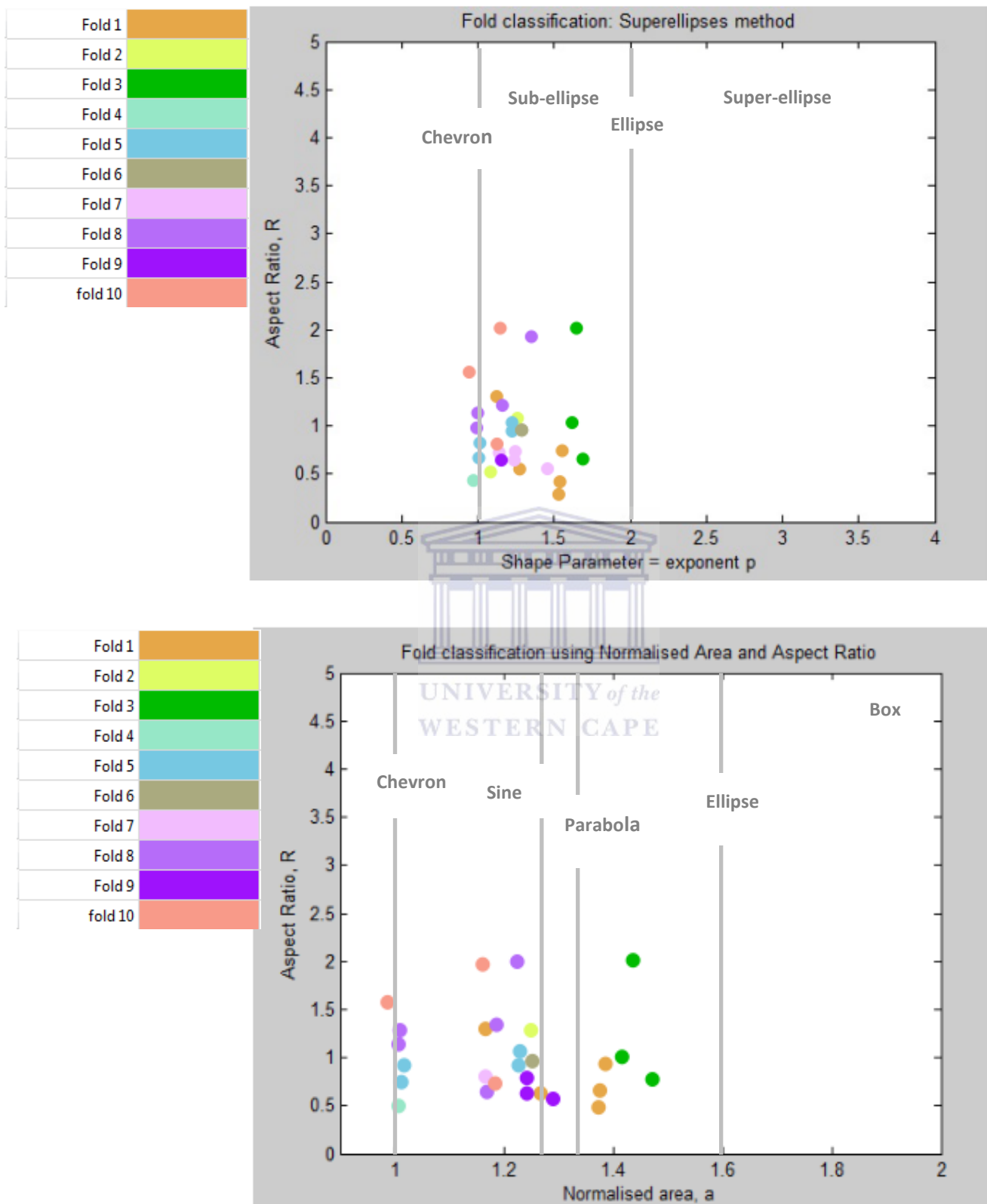


Fig. 5.10. Analysis of the **Folds 1-10** using Sub-ellipses and Super-ellipses method. (a) graph of the aspect ratio versus the shape parameter  $p$ ; (b) graph of the aspect ratio versus the normalised area.

Table.5.4 Fold shape parameter obtained from Sub-ellipses and Super-ellipses method

	Fold 1						Fold 2			Fold 3		Fold 4
Fold Limb (fl)	$f_{1 2}$	$f_{1 2}$	$f_{1 2}$	$f_{1 4}$	$f_{1 5}$	$f_{1 6}$	$f_{2 1}$	$f_{2 2}$	$f_{2 3}$	$f_{3 1}$	$f_{3 2}$	$f_{4 1}$
Shape Parameter(L)	0.3636	0.5051	0.5455	0.5657	0.8081	0.4848	0.4848	0.4848	0.4848	0.6869	0.8687	0.8687
Normalised area (a)	1.2182	1.2182	1.3273	1.3394	1.4848	1.2909	1.2909	1.2909	1.2909	1.4121	1.5212	1.5212
Aspect ratio (R)	0.6455	0.7552	0.4157	0.4172	0.7195	0.7193	0.7474	0.3523	0.8788	0.8295	0.8467	0.9408
Interlimb Angle	89.1849	66.4817	95.1173	92.3134	29.8687	71.2194	69.1548	111.295	60.7583	41.3644	17.6323	15.8914

	Fold 5			Fold 6	Fold 7	Fold 8	Fold 9			Fold 10		
Fold Limb (fl)	$f_{5 1}$	$f_{5 2}$	$f_{5 3}$	$f_{6 1}$	$f_{7 1}$	$f_{8 1}$	$f_{9 1}$	$f_{9 2}$	$f_{9 3}$	$f_{9 4}$	$f_{10 1}$	$f_{10 2}$
Shape Parameter	0.1818	0.2020	0.4848	0.0808	0.4848	0.4848	0.3838	0.4848	0.5051	0.3434	0.5455	0.4848
Normalised area (a)	1.1091	1.1212	1.2909	1.0485	1.2909	1.2902	1.2303	1.2909	1.3030	1.2061	1.3273	1.2909
Aspect ratio (R)	1.3767	1.2319	0.8164	0.5912	0.4811	1.3624	1.2000	0.7309	0.4924	0.7614	0.4353	0.6911
Interlimb(L) Angle	61.4481	65.8690	64.5065	114.5003	93.9210	41.4263	54.3581	70.3534	90.2968	81.5405	92.4814	73.4046



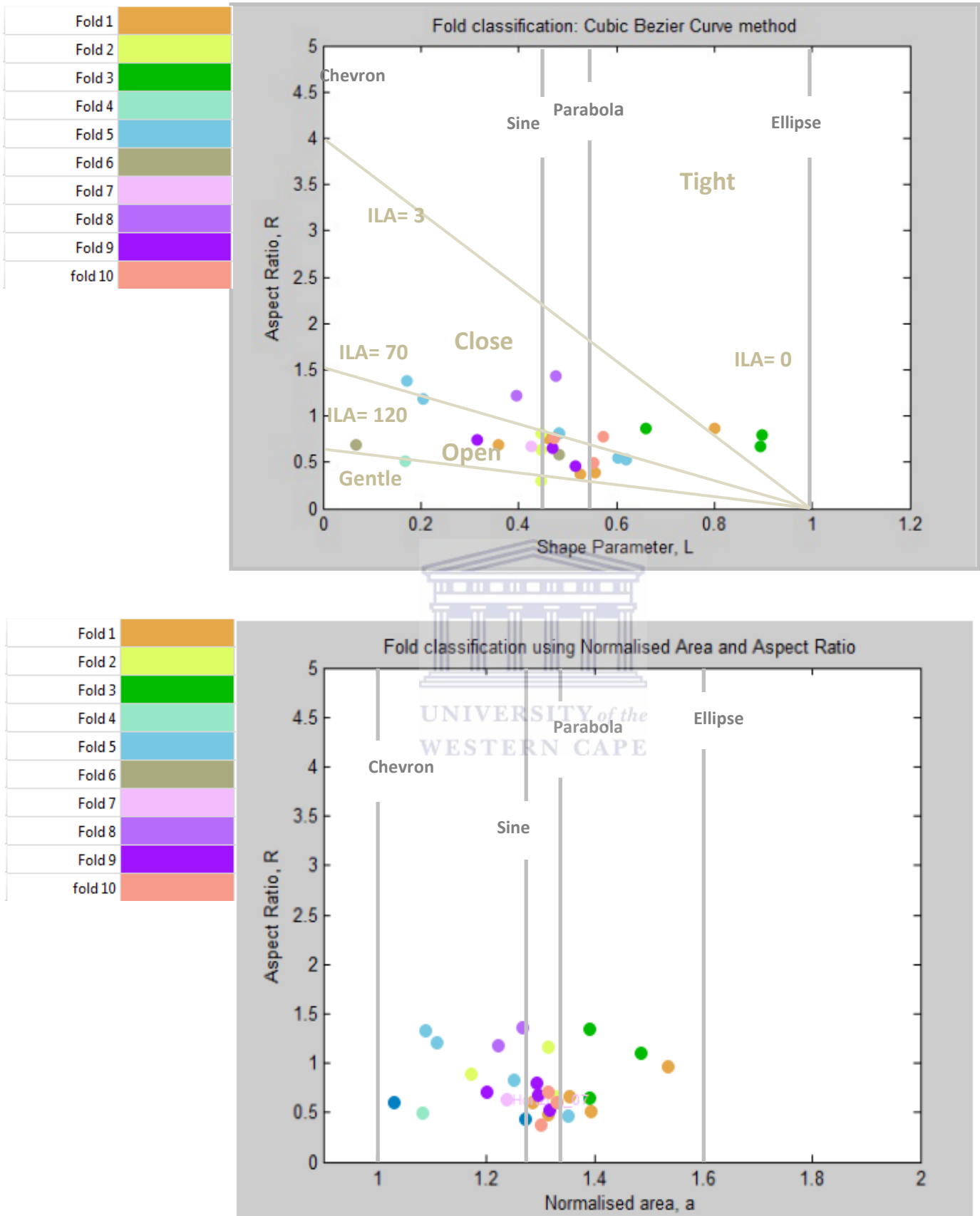


Fig. 5.11. Analysis of the Folds 1-10 by Fold Profiler using Cubic Bézier curves method. (a) Graph of the aspect ratio versus the shape parameter L; (b) graph of the aspect ratio versus the normalised area.

# Chapter 6

## Mathematical Modelling of Fold Kinematic Mechanisms and Simulation of Strain Pattern

### 6.1 Introduction

Four mechanisms associated with fold deformations are common in structural geology: Initial Layer Shortening (ILSH), Tangential Longitudinal Strain (TLS), Flexural Flow (FF) and flattening (FL). Kinematic folding mechanisms reflect the different way folded layers accommodate strain. Structural geologists are often able to infer one or two kinematic folding mechanisms involved in the folding process by interpreting field data from natural folds. However the task becomes more complicated when it comes to infer the strain pattern. The strain pattern is the combination of kinematic folding mechanism responsible of the bulk strain accommodate by the folded layer during folding. The strain pattern cannot be observed in the field instead it can be determined using use numerical modelling. In the previous chapter we have determined the geometrical parameters that control the shape of the folds of interest, in this chapter we are going to first describe the mathematical aspect of the different kinematic folding mechanisms; secondly we are going to simulate theoretical folds by superimposing the different kinematic fold mechanism using a Mathematical code called FoldModeler (Batisda et al., 2003; Bobillo-Ares et al., 2004). The main objective is to simulate theoretical folds which best fit the geometrical parameters of natural folds analysed in Chapter 5.

## 6.2 Mathematical Description of Kinematic Folding Mechanisms

### 6.2.1 Tangential Longitudinal Strain (TLS)

During tangential longitudinal strain (TLS) the outer part of the fold is stretched and the inner part is compressed. In the TLS the guide line (GL) is always a Neutral Line (Aller et al., 2004). Fig.6.1a shows the image  $Q_t$  of an initial point  $Q$ ; respectively located on  $GL_t$  and GL.

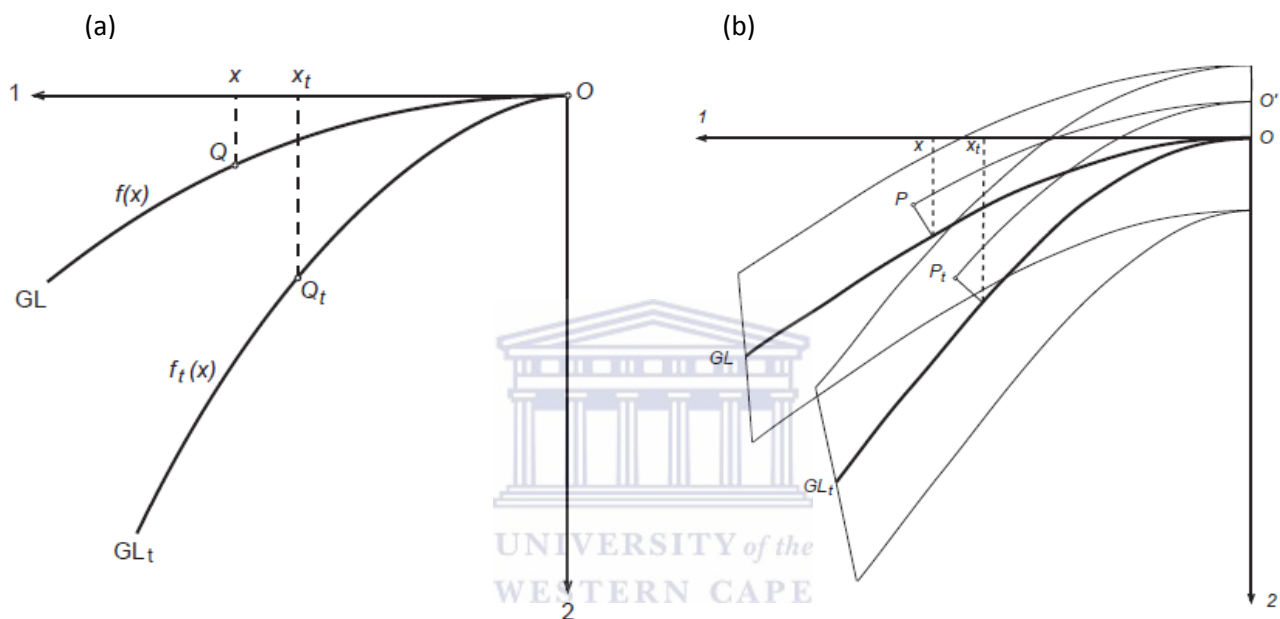


Fig.6.1. (a) Geometrical changes experienced by the Guide Line (GL) during Tangential Longitudinal Strain (TLS). (b) Geometrical changes experienced by the Guide Line (GL) during Flexural Flow (FF)(Aller et al., 2004).

One of the conditions of this mechanism is that the arc length  $OQ_t$  is equal to arclength  $OQ$ .

$x_t$  is calculated using the following differential equation:

$$\frac{dx_t}{dx} = \sqrt{\frac{1+f'(x)^2}{1+f'_t(x)^2}}; \quad x_t(0)=0 \quad (50)$$

$f'(x)$  is the derivative of  $f(x)$ .  $f_t(x)$  and  $f(x)$  are functions corresponding to GL and  $GL_t$ . In case the image  $P_t(x_t h_t)$  of a point  $P(x, h)$  is not located on the Neutral Line (NL), the solution of Eq.(50) is still  $x_t$  and  $h_t$  is

$$h_t = \frac{h(2+hk)}{1+\sqrt{1+k_t h(2+hk)}} \quad (51)$$

Where  $k_t$  and  $k$  are the curvatures of  $Q$  and  $Q_t$  respectively:

$$k = \frac{f''(x)}{(1+[f'(x)^2])^{3/2}} \quad ; \quad k_t = \frac{f''(x)}{(1+[f'(x)^2])^{3/2}} \quad (52)$$

### 6.2.2 Flexural Flow (FF)

During TLS the strain is concentrated in the hinge of the fold, whereas the strain is concentrated on limbs when the fold accommodates strain by FF. During FF the lines parallel to the GL do not experience any change in length. Fig.6.1b shows a layer folded by FF. FF relies on two conditions; firstly all the points inside the folded layer remain at the same distance from the GL and secondly arc length  $OP_t$  is equal arclength  $OP$ (Fig.6.1b).  $x_t$  is calculated as follows:

$$\frac{dx_t}{dx} = \frac{|r'(x)|}{|r_t'(x)|} \quad x_t(0)=0 \quad (53)$$

With  $[r(z) = [ze_1 + f(z)e_2 + n(z)h, \quad (54)$

$$n(z) = \frac{\text{sign}[f''(z)]}{\sqrt{1+f'(z)^2}} [f'(z)e_1 - e_2], \quad (55)$$

$$[r_t(z) = [ze_1 + f_t(z)e_2 + n_t(z)h, \quad (56)$$

$$\mathbf{n}(z) = \frac{\text{sign}[f_t''(z)]}{\sqrt{1 + f_t''(z)^2}} [f_t'(z)e_1 - e_2]$$

### 6.2.3 Initial Layer Shortening (ILSH) and Flattening (FL)

During flattening or initial layer shortening of the GL (Fig.7.2), the coordinates of  $p$  change from  $p(x, g(x))$  to  $p(x', f(x'))$ . The latter are related to the former through the following equation:

$$x' = \sqrt{\lambda_1}x \text{ and } y' = \sqrt{\lambda_2}y$$

$\sqrt{\lambda_1}$  and  $\sqrt{\lambda_2}$  are the stretches of flattening

$y' = \sqrt{\lambda_1}y$  can be written as follows:

$$f(x') = \sqrt{\lambda_1} g(x) \text{ or } g(x) = \frac{1}{\sqrt{\lambda_1}} f(x')$$

The length  $l_o$  of the flattened guideline is as follows:

$$l_o = \frac{2}{\sqrt{\lambda_2}} \int_0^{x'_0} \sqrt{1 + \frac{\lambda_2}{\lambda_1} f'(x')^2} dx'; \quad f'(x) \text{ being the derivative of } f(x)$$

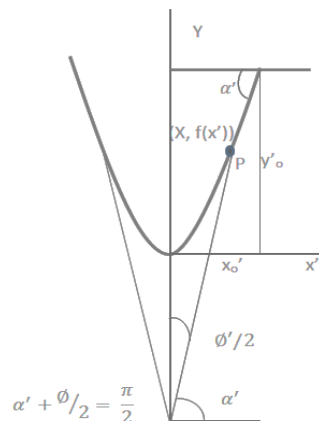


Fig.6.2. Geometrical changes experienced by the Guide Line (GL) Flattening (FL) or Initial Layer shortening (ILSH) (Aller et al., 2008).

## 6.2 Numerical Simulation of folds

The simulation of folds aims to decipher the strain pattern or the sequence of kinematic folding mechanisms responsible for the strain accommodation in the folds analysed in chapter four. Theoretical folds are generated by “a trial and error” method, the process is repeated until the numerical fold that best fit the natural fold under consideration is found. FoldModeler developed in *the MATHEMATICA<sup>TM</sup>* environment (Batisda et al., 2003; Bobillo-Ares et al., 2004) is used to determine the sequential strain pattern responsible for strain accommodation. The first step in the 2D numerical modelling of a fold is to define the initial configuration of the layer profile that will be folded. The layer profile is divided into a grid of quadrilaterals that are small enough to assume nearly homogeneous strain within them (Batisda et al., 2004). The folded layer is characterised by the following (Fig.6.3):

- Folded layer: {**parameters, grid**};
- Segment: {**leftPoint, right Part**}
- Point: {**x, y**} or {**x, h**}

The Function called “**Parameters**” represents a list of parameters describing the Guide Line (GL) such as:

- e: Eccentricity of the conic representing the guideline.
- a: Scale factor. Its value must be very high if we want to obtain a flat layer.
- e1: Base length of the quadrilaterals.
- e2: Height length of the quadrilaterals.
- Grid: {**upper Part, lower Part**}



The following step after setting up the parameter controlling the GL is to draw the fold. This is done by applying the function strain [**iniGrid, Program1**] to the initial layer.

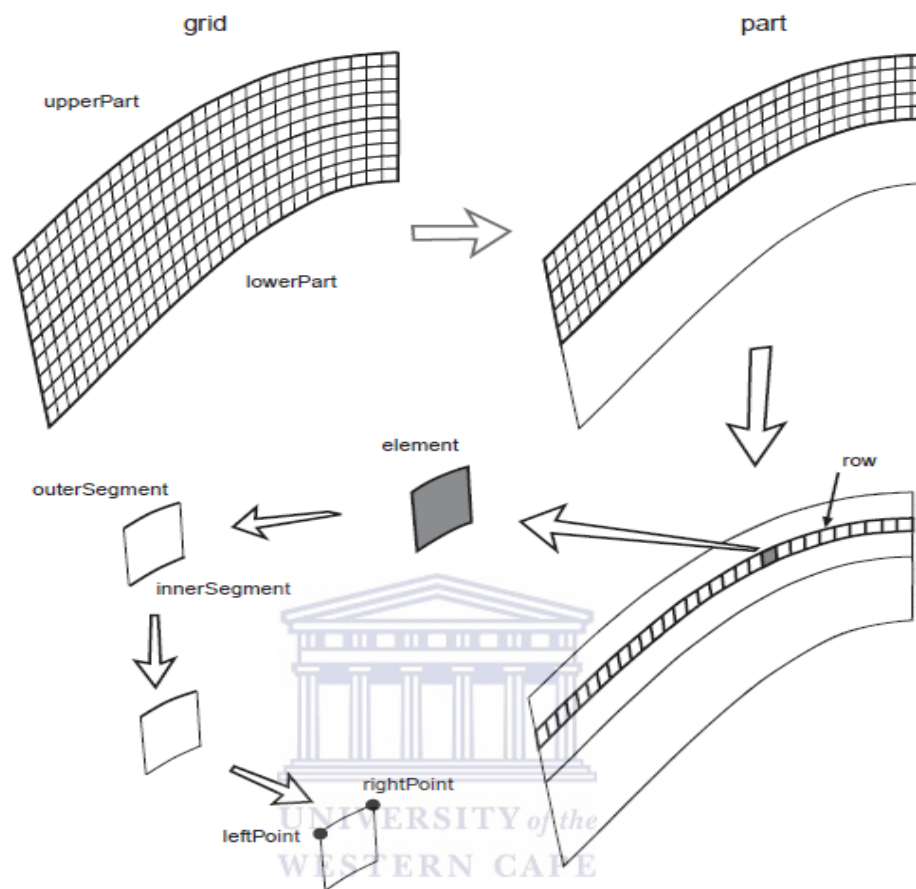


Fig.6.3 Elements used in the numerical modelling of a Fold (Aller et al., 2004)

The function **Program1** is composed of folding blocks, each block can be described as follows:

**block**={N, h-increment, e-increment} "N" is the number that indicates the mechanism ( 1-Tangential Longitudinal Strain without area change, 2-Flexural Flow , 3-Homogeneous Strain) "h-increment" is a number that indicates the h (aspect ratio) increment in the fold limb during that folding step, "e-increment" is a number that indicates the increment of the guideline eccentricity during that folding step. **Program 1** is written as follows: **program1 = {block1, block2, block3 ...}**. The blocks involved in **Program 1** can be defined as follows:

**block1 = {2, {1, 0.5, 0}};**

**block2 = {1, {4, 0.5, 0}, {2, 0.5, 0}}**

**block3 = {2, {3, matrix2}}**

Block 1 involves a single even strain pattern (TLS) that will be executed twice successively.

Block 2 involves a sequence of two strain patterns (TLS strain without area change and FF)

that will be executed once. Block 3 involves a single homogeneous strain. **Matrix 1** describes homogeneous strain resulting from pure shear.

The output obtained by the application of the strain pattern sequence **program 1** is a fold limb since the fold shape parameters obtained in Chapter 5 were computerized from fold limbs. Other outputs are:

- The bulk shortening of the fold
- Final aspect ratio of GL
- Final length of GL
- Layer boundary at the hinge, amplitude of the convex boundary of the folded layer and the ratio between the two parameters.

### 6.3 Results and Interpretations

Folds (Fig.4.6) of metric scale that formed during the second phase of deformation of the Warm Zand Structure were simulated using the method mentioned above. Each individual theoretical fold obtained shows a particular strain pattern. Fig.6.4b and Fig.6.4c show a folded configuration of theoretical layers that best fit Fold 1 shape parameters. The sequence starts with TLS followed by FF and finally ending with FL .



(b)  
**matrix** = {0.8, 1.0}  
**block1** = {1, {1, 0.5, 0}}  
**block2** = {1, {2, 0.25, 0}}  
**block3** = {1, {3, matrix1}}  
**program1** = {block3, block1, block2};

	Theoretical fold limb $f_1l_2$	Natural fold limb $f_1l_2$
Aspect ratio(R)	0.7500	0.7396
Eccentricity(e)	0.8894	0.8919

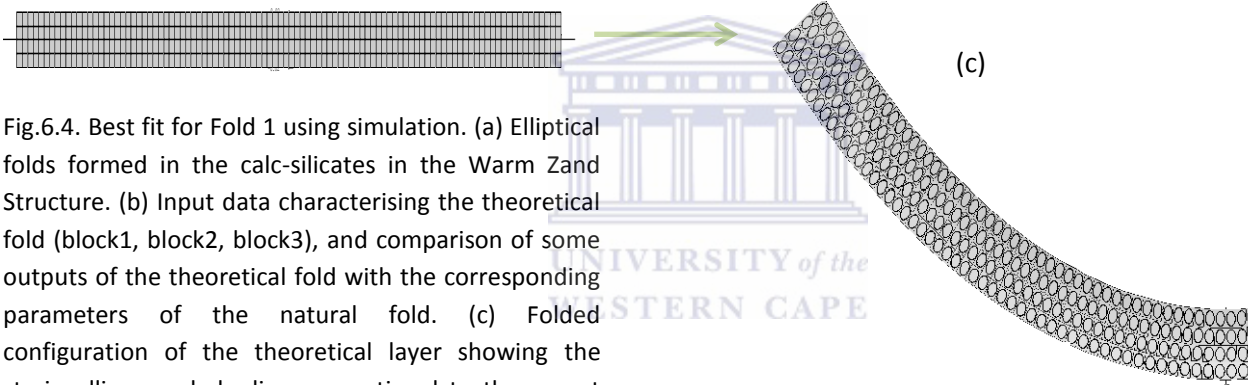
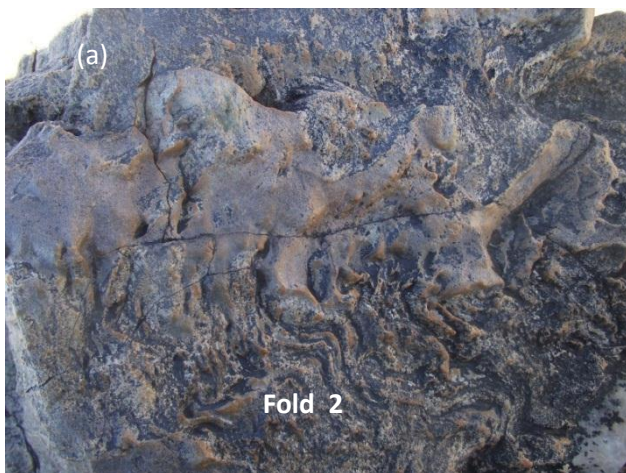


Fig.6.4. Best fit for Fold 1 using simulation. (a) Elliptical folds formed in the calc-silicates in the Warm Zand Structure. (b) Input data characterising the theoretical fold (block1, block2, block3), and comparison of some outputs of the theoretical fold with the corresponding parameters of the natural fold. (c) Folded configuration of the theoretical layer showing the strain ellipse and shading proportional to the aspect ratio of the strain ellipses.



(b)  
**matrix** = {0.8, 1.0}  
**block1** = {1, {1, 0.5, 0}};  
**block3** = {1, {3, matrix1}};  
**program1** = {block3,block1, block3 }

	Theoretical fold limb $f_2l_2$	Natural fold limb $f_2l_2$
Aspect ratio(R)	0.7812	0.7626
Eccentricity(e)	1.0000	1.0000

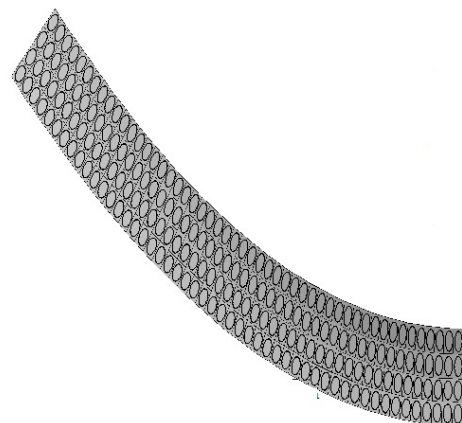
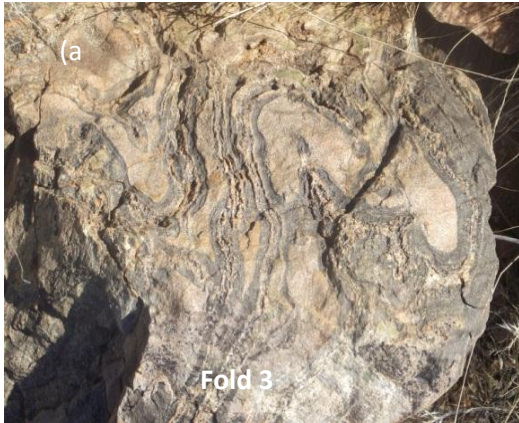


Fig.6.5. Best fit for natural Fold 2 using simulation. (a) Parabolic folds formed in the calc-silicates in the Warm Zand Structure. (b) Input data characterising the theoretical fold (block1, block2, block3), and comparison of some outputs of the theoretical fold with the corresponding parameters of the natural fold. (c) Folded configuration of the theoretical layer showing the strain ellipse and shading proportional to the aspect ratio of the strain ellipses.



**matrix** = {0.8, 1.0} (b)  
**block1** = {1, {1, 0.7, 0}}  
**block2** = {1, {2, 0.6, 0}}  
**block3** = {1, {3, matrix1}}  
**program1** = {block3, block1, block2}

	Theoretical fold limb $f_3l_2$	Natural fold limb $f_3l_2$
Aspect ratio(R)	0.9233	0.9333
Eccentricity(e)	1.3000	1.3627
Theoretical bulk shortening: 53.99%		

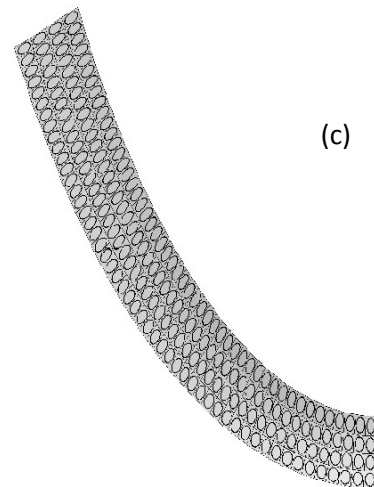
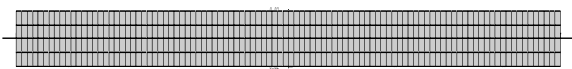
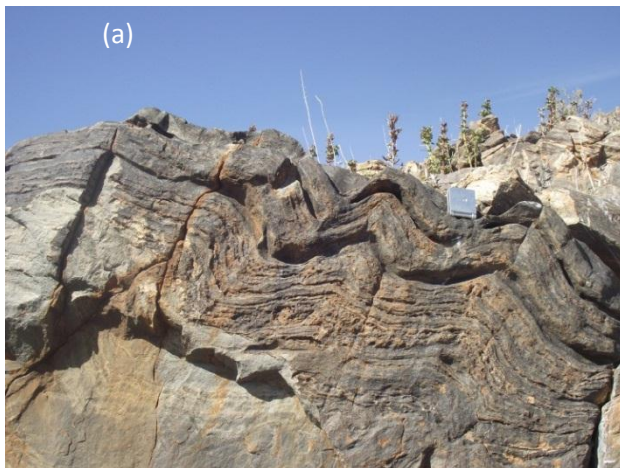
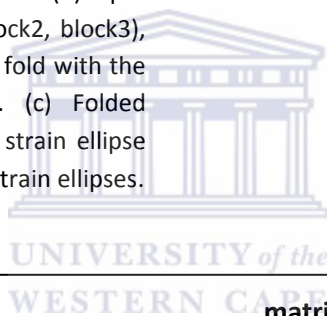


Fig.6.6. Best fit for Fold 3 using simulation. (a) Hyperbola folds formed in the calc-silicates in the Warm Zand Structure. (b) Input data characterising the theoretical fold (block1, block2, block3), and comparison of some outputs of the theoretical fold with the corresponding parameters of the natural fold. (c) Folded configuration of the theoretical layer showing the strain ellipse and shading proportional to the aspect ratio of the strain ellipses.



**matrix** = {0.8, 1.0} (b)  
**block1** = {1, {1, 0.5, 0}}  
**block3** = {1, {3, matrix1}}  
**program1** = {block3, block2, block3}

	Theoretical fold limb $f_9l_1$	Natural fold limb $f_9l_1$
Aspect ratio(R)	0.9839	0.9761
Eccentricity(e)	1.000	1.1026

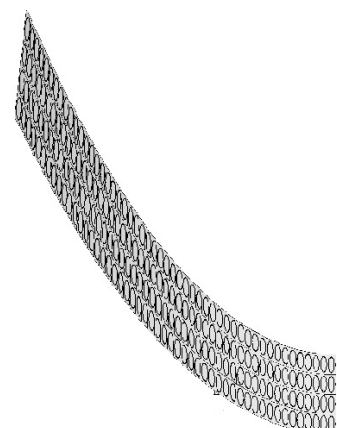
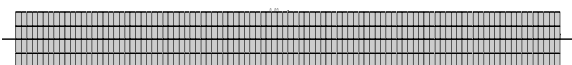


Fig.6.7. Best fit for Fold 9 using simulation. (a) Parabolic folds formed in the calc-silicates in the Warm Zand Structure. (b) Input data characterising the theoretical fold (block1, block2, block3), and comparison of some outputs of the theoretical fold with the corresponding parameters of the natural fold. (c) Folded configuration of the theoretical layer showing the strain ellipse and shading proportional to the aspect ratio of the strain ellipses.



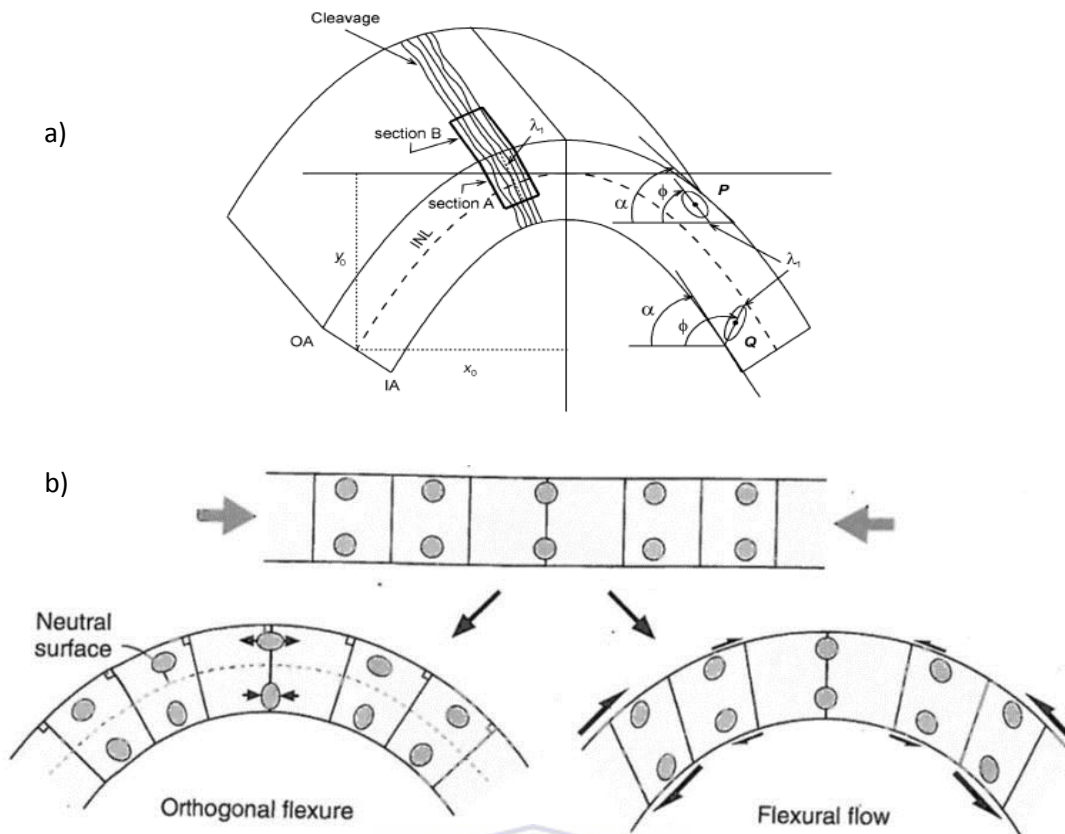


Fig. 6.8.(a) Location of strain data used to constraint numerical models. The data must be sampled on the hinge and limbs of the fold. Point Q and P represent strain marker at inner arc and outer respectively. Section A shows the position of cleavage on the hinge (Toimil and Fernández, 2007). (b) Deformation pattern of pebbles deformed by Tangential Longitudinal Strain or orthogonal flexure and Flexural Flow (Fossen, 2010, p. 233)

UNIVERSITY of the  
WESTERN CAPE

The intensity of FF (0.25) is less significant than that of TLS (0.5) and FL (0.8). This may implies that the folding process of theoretical Fold 1 is dominated by TLS and FL; as a result the strain is more concentrated in the hinge.

Fig.6.5a and Fig6.7b show the folded configuration of theoretical layers that best fit Fold 2 and Fold 9 shape parameters. The sequences start with ILSH follows by TLS and finally ending with FL. Although the configurations of theoretical Fold 2 and Fold 9 appear to be similar, the value of the eccentricity of their respective guide line  $GL_2$  ( $e=0.8$ ) and  $GL_9$  ( $e=0.9$ ) differs as set out above.

The configuration of the theoretical fold which best fits Fold 3 (Fig.6.6b) displays a strain pattern starting with TLS followed by FF and ending with FL. Intensities of TLS (0.7) and FF (0.6) indicate that the strain is nearly equally distributed in the hinge and in the limb of theoretical Fold 3.

From the theoretical folds obtained from the simulation of folds, we observed that TLS and FL are necessary for all cases whereas, FF is only necessary in some cases.

The models of strain pattern sequence by which the analysed folds accommodate strain pose some drawbacks. Several good fits for each analysed fold can be obtained apart from the ones displayed above. Hence the same finite strains and models can be the result of a diversity of deformation histories.

To reduce the number of possible fits and thus constrain the models, strain data must be collected from the hinge zones (cleavages) and from limbs (deformed pebbles for instance) of natural folds (Fig. 6.8a). The strain data sampled at the limb should be located at inner arc and outer arc of the fold as the shape of the strain markers found in folds are formed according to folding kinematic mechanisms. In Fig.6.8b pebbles deformed by TLS or orthogonal flexure show different deformation pattern in the inner and outer arc of the fold whereas the pebbles deformed by FF show more or less the same deformation pattern in the inner and outer arc of the fold. We were not able to find any strain markers located at hinges or limbs of folds while mapping the Warm Zand Structure. Hence while the numerical models demonstrated that the ISHL, TLS, FF and FL controlled the formation of folds in the study area, they (models) may not represent the correct deformation pattern or the correct order in which the different mechanisms occurred during the folding process as the necessary controls could not be performed due to the absence of suitable strain markers. van Bever Donker(1980) assumed that ISHL took place during the folding process and that

when the bulk shortening exceed 23% FL occurred. The results we found shows that in addition to ISHL and FL, TLS and FF may have also took place. However the order in which they occurred was not found in this study.





---

# Chapter 7

---

## Conclusions

This research project had two different parts: The first was about the mapping of a section of the Warm Zand Structure and the collection of strain data. The second part focused on the analysis of the finite strain and strain pattern in the Warm Zand Structure. The Warm Zand Structure consists of strongly deformed calc-silicates of the Puntsit formation and feldspathic quartzites of the Goede Hoop formation which gradually change into pure quartzites in some locations. The second phase of folding  $F_2$  in the calc-silicates gave open folds. Strain markers are very scarce in the Warm Zand Structure; on the Emmanuel Farm pebbles were not found. However on the Compion Farm, pebbles are scattered and occur in few number. In the study area boudins were found in loose rocks hence they could not be used to estimate orientation of the XY plane of the strain ellipsoid (Ramsay, 1967). Folds on the other hand was common and was used to investigate the bulk shortening of the rocks and to understand the kinematical folding mechanisms involved in the folding process of the rock in the Warm Zand Structure. The strain contour map and the Sherwin and Chapple graph were used to investigate the strain and viscosity contrast respectively. The viscosity contrast of the folds collected in the Puntsit falls between 100-53 whereas the bulk shortening on the other hand is between 60-53%. The values of the shortening found agree with those found by van Bever Donker (1980). The numerical modelling on the other demonstrated that in addition to layer parallel shortening and the flattening mention by van Bever Donker(1980) Tangential Longitudinal Strain and Flexural Flow are also involved in the folding process of the fold collected in the Puntsit Formation.

## 7.1 Future Research

The idea of this research topic came to our mind while reading the PhD thesis of Professor Jan van Bever Donker. During his PhD project, Professor Jan van Bever Donker mapped the Kakamas terrane, but provided little information regarding the evolution of the strain in the area because of the limited resources available at that time to perform such analyses. One of the future avenues of this research will therefore be to use the strain contour map to study the distribution of strain in the whole Kakamas terrain. Another avenue of research will be to create robust numerical models in order to improve the models of strain pattern created during this study.



## REFERENCES

- Dalziel, I.W.D. (1991). Pacific margins of Laurentia and East Antarctica-Australia as a conjugate rift pair: Evidence and implications for an Eocambrian supercontinent. *Journal of Geology* 19(6), 598-601.
- Abbassi, M. R., & Mancktelow, N. S. (1992). Single layer buckle folding in non-linear materials—I. experimental study of fold development from an isolated initial perturbation. *Journal of Structural Geology*, 14(1), 85-104.
- Aller, J., Bobillo-Ares, N. C., Bastida, F., & Lisle, R. J. (2008). Total bulk strain in flattened parallel folds. *Journal of Structural Geology*, 30(7), 827-838.
- Aller, J., Bastida, F., Toimil, N. C., & Bobillo-Ares, N. C. (2004). The use of conic sections for the geometrical analysis of folded surface profiles. *Tectonophysics*, 379(1), 239-254.
- Bastida, F., Aller, J., & Bobillo-Ares, N. (1999). Geometrical analysis of folded surfaces using simple functions. *Journal of Structural Geology*, 21(7), 729-742.
- Bastida, F., Bobillo-Ares, N., Aller, J., & Toimil, N. (2003). Analysis of folding by superposition of strain patterns. *Journal of Structural Geology*, 25(7), 1121-1139.
- Bastida, F., Aller, J., Bobillo-Ares, N. C., & Toimil, N. C. (2005). Fold geometry: A basis for their kinematical analysis. *Earth-Science Reviews*, 70(1), 129-164.
- Biot, M.A. (1965). *Mechanics of incremental deformations*. Wiley, New York.
- Biot, M. A. (1961). Theory of folding of stratified viscoelastic media and its implications in tectonics and orogenesis. *Geological Society of America Bulletin*, 72(11), 1595-1620.
- Bobillo-Ares, N., Bastida, F., & Aller, J. (2000). On tangential longitudinal strain folding. *Tectonophysics*, 319(1), 53-68.

- Bobillo-Ares, N., Toimil, N., Aller, J., & Bastida, F. (2004). FoldModeler: A tool for the geometrical and kinematical analysis of folds. *Computers & Geosciences*, 30(2), 147-159.
- Chapple, W. M. (1968). A mathematical theory of Finite-Amplitude Rock-Folding. *Geological Society of America Bulletin*, 79(1), 47-68.
- Claus, G., & Schlegel, J. (1991). The metamorphic and structural evolution of the Kheis tectonic province. *Bulletin of the Precambrian Research Unit, University of Cape Town, South Africa*, 36, 50-59.
- Cornell, D.H., Thomas, R.J., Gibson, R., Moen, H.F.G., Moore, J.M., & Reid D.L. ( 2006). Namaqua-Natal Province. In: M.R. Johnson, C.R. Anhaeuser & R.J. Thomas, (Eds.), *Geology of South Africa. Geological Society South Africa and Council for Geoscience*, Pretoria, 343-347
- Currie, J., Patnode, H., & Trump, R. (1962). Development of folds in sedimentary strata. *Geological Society of America Bulletin*, 73(6), 655-673.
- Dahlstrom, C. (1969). Balanced cross sections. *Canadian Journal of Earth Sciences*, 6(4), 743-757.
- De Paor, D. G. (1996). Bézier curves and geological design. *Computer Methods in the Geosciences*, 15, 389-417.
- Dieterich, J. H., & Carter, N. L. (1969). Stress-history of folding. *American Journal of Science*, 267(2), 129-154.
- Fletcher, R. C. (1974). Wavelength selection in the folding of a single layer with power-law rheology. *American Journal of Science*, 274(9), 1029-1043.
- Fletcher, R., & Sherwin, J. (1978). Arc lengths of single layer folds; a discussion of the comparison between theory and observation. *American Journal of Science*, 278(8), 1085-1098.

Gardiner, M. (1965). The superellipse: A curve that lies between the ellipse and the rectangle. *Scientific American*, 213(3), 222-232.

Geringer, G. (1973). *Die geologie van die argeïese gesteentes en jonger formasies in die gebied wes van upington met spesiale verwysing na die verskillende graniet-voorkomste*. Unpublished PhD, University of the Orange Free State, Bloemfontein. 203 pp.

Hudleston, P. J., & Stephansson, O. (1973). Layer shortening and fold-shape development in the buckling of single layers. *Tectonophysics*, 17(4), 299-321.

Hudleston, P. (1973). An analysis of "single-layer" folds developed experimentally in viscous media. *Tectonophysics*, 16(3), 189-214.

Hudleston, P. J., & Lan, L. (1995). Rheological information from geological structures. *Pure and applied Geophysics*, 145(3-4), 605 – 620.

Lisle, R. J. (1988). The superellipsoidal form of coarse clastic sediment particles. *Mathematical Geology*, 20(7), 879-890.

Lisle, R. J., Fernández Martínez, J. L., Bobillo-Ares, N., Menéndez, O., Aller, J., & Bastida, F. (2006). FOLD PROFILER: A MATLAB—based program for fold shape classification. *Computers & Geosciences*, 32(1), 102-108.

Liu, C., Zhang, Y., & Wang, Y. (2009). Analysis of complete fold shape based on quadratic bézier curves. *Journal of Structural Geology*, 31(6), 575-581.

Mase, G. E. (1970). *Schaum's outline of theory and problems of continuum mechanics*. McGraw-Hill, New York.

- Matthews, P., Bond, R., & Van den Berg, J. (1974). An algebraic method of strain analysis using elliptical markers. *Tectonophysics*, 24(1), 31-67.
- Moen, H.F.G. (2007). *The geology of the upington area, explanation 1,250 000 sheet 2820, Council for Geoscience*. Pretoria.
- Ramberg, H. (1962). Contact strain and folding instability of a multilayered body under compression. *Geologische Rundschau*, 51(2), 405-439.
- Ramsay, J. (1967). *Folding and fracturing of rocks*. New York: McGraw-Hill
- Ramsay, J. G., & Huber, M. (1987). *Modern structural geology, volume 2: Folds and fractures*. Academic Press, London.
- Robb, L., Armstrong, R., & Waters, D. (1999). The history of granulite-facies metamorphism and crustal growth from single zircon U–Pb geochronology: Namaqualand, south africa. *Journal of Petrology*, 40(12), 1747-1770.
- Schmalholz, S. M., & Podladchikov, Y. Y. (2000). Finite amplitude folding: Transition from exponential to layer length controlled growth. *Earth and Planetary Science Letters*, 179(2), 363-377.
- Schmalholz, S. M., & Podladchikov, Y. Y. (2001). Strain and competence contrast estimation from fold shape. *Tectonophysics*, 340(3), 195-213.
- Schmalholz, S. M., & Podladchikov, Y. Y. (2001). Strain and competence contrast estimation from fold shape. *Tectonophysics*, 340(3), 195-213.
- Sherwin, J., & Chapple, W. M. (1968). Wavelengths of single-layer folds; a comparison between theory and observation. *American Journal of Science*, 266(3), 167-179.

- Shimamoto, T., & Ikeda, Y. (1976). A simple algebraic method for strain estimation from deformed ellipsoidal objects. 1. basic theory. *Tectonophysics*, 36(4), 315-337.
- Srivastava, D. C., & Lisle, R. J. (2004). Rapid analysis of fold shape using bézier curves. *Journal of Structural Geology*, 26(9), 1553-1559.
- Srivastava, D. C., & Lisle, R. J. (2004). Rapid analysis of fold shape using bézier curves. *Journal of Structural Geology*, 26(9), 1553-1559.
- Thomas, R., Cornell, D., Moore, J., & Jacobs, J. (1994). Crustal evolution of the namaqua-natal metamorphic province, southern Africa. *South African Journal of Geology* 97, 8-14.
- Truesdell, C., & Toupin, R. (1960). The classical field theories. In: S. Flugge (Ed.), *The Encyclopedia of Physics* (vol. 3, pp. 226-793). Berlin: Springer.
- Van Bever Donker, J. (1980). Structural and Metamorphic Evolution of an Area around Kakamas and Keimoes, Cape Province, South Africa. *Precambrian Research Unit, University of Cape Town*, 28, 165pp.
- Van Bever Donker, J (1983). The Neusspruit lineament, Upington Geotraverse, possible boundary between the Namaqualand Metamorphic Complex and the Namaqua front. In Botha, B.J.V: Namaqualand Metamorphic Complex. *Special Publication of the Geological Society of South Africa* 10, 193-198.
- Van Zyl, C. Z. (1981). Structural and metamorphic evolution in the transitional zone between craton and mobile belt, Upington Geotraverse. *Precambrian Research Unit, University of Cape Town*, 31, 87-103.